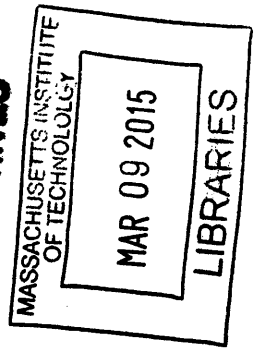

Impeller Loss Reduction in Multi-Stage Centrifugal Compressors

by

Kristina Barile

Bachelor of Science Highest Honors, Engineering Sciences, Mechanical and Material Sciences, Harvard University, 2012

Submitted to the Department of Aeronautics and Astronautics in partial fulfillment of the requirements for the degree of

Master of Science in Aeronautics and Astronautics

at the

MASSACHUSETTS INSTITUTE OF TECHNOLOGY

February 2015

Signature redacted

Author.....

Department of Aeronautics and Astronautics

October 3, 2014

Certified by..... Signature redacted .....

Edward M. Greitzer

H.N. Slater Professor of Aeronautics and Astronautics

Thesis Supervisor

Accepted by..... Signature redacted .....

Paulo C. Lozano

Associate Professor of Aeronautics and Astronautics

Chair, Graduate Program Committee

Impeller Loss Reduction in Multi-Stage Centrifugal Compressors

by

Kristina Barile

Bachelor of Science Highest Honors, Engineering Sciences, Mechanical and Material Sciences, Harvard University, 2012

Submitted to the Department of Aeronautics and Astronautics on October 3, 2014, in partial fulfillment of the requirements for the degree of Master of Science in Aeronautics and Astronautics

Abstract

Loss generation features for the first stage impeller in a multistage centrifugal compressor are examined using three-dimensional RANS computations. The calculations were carried out for a baseline configuration and for seven other impeller configurations, with the constraints of constant mass flow and constant work per unit mass flow. The computations showed an 8 percent reduction in loss, compared to the baseline, for a configuration that incorporated 60% of the total casing blade angle change in the front 20% chord. Two-dimensional interactive boundary layer computations were carried out to demonstrate links between the loss variation and the changes in boundary layer behavior in the front 20% of the blade passage.

Thesis Supervisor: Edward M. Greitzer
Title: H.N. Slater Professor of Aeronautics and Astronautics

Acknowledgments

Firstly, I would like to thank my advisor, Professor Edward Greitzer, for his guidance and mentorship during my stay at MIT. Your passion for your work is tangible, and it was a privilege to work with you. Thank you for your dedication to the project and, most especially, for challenging me to think critically about each decision made and the message being conveyed. I know this will come in handy in all my future work, and I am very appreciative for that.

I am grateful for the continued support of Dr. Michael Casey, whose industrial experience was invaluable to the project. Thank you for your useful feedback during our regular interactions, for your insight and support, and for occasionally sharing a photo of your artistic endeavors with us. I would also like to thank Claudio Lettieri for always having an open door to my seemingly endless questions. Thank you for sharing your experience and knowledge with me.

I would like to thank Mitsubishi Heavy Industries for sponsoring this project. I am very grateful to have had the opportunity to work with Dr. Eisaku Ito and Dr. Akihiro Nakaniwa. Thank you for your patience and understanding, and also your helpful comments and suggestions throughout this project.

I am also thankful to the GEM Foundation and the National Science Foundation (NSF) for helping to fund my graduate experience.

Last but not least, I am especially grateful for the support of my family, friends, and labmates, for always being there when I needed them most.

Contents

1 Introduction 10
1.1 Background and Motivation 10
1.2 Impeller Geometry and Flow Features 11
1.3 Nomenclature 13
1.4 Previous Work 13
1.5 Research Questions 14
1.6 Thesis Contributions 14
2 Implementation 16
2.1 Computational Approach 16
2.1.1 ANSYS CFX 16
2.1.2 MISES 18
2.2 Mesh Generation 18
2.3 Boundary Conditions 18
2.4 Performance Metrics 19
3 Characteristics of Baseline Impeller Flow 20
3.1 Loss Production in Impeller 20
4 Blade Geometry Assessment 23
4.1 Case Study Motivation and Parameters 23
4.2 Blading Examined 24
4.3 Loss Production Correlations with Blading 25
4.3.1 Overall Loss Trends 25
4.3.2 Locating Loss Generation Regions 27
4.3.3 Local Loss Trends 28
4.4 Mesh Refinement Analysis 31
4.5 Chapter Summary 33
5 Inlet Dissipation 34
5.1 Motivation. 34
5.2 Effect of Inlet Shape 36
5.2.1 Inlet 2 Entropy Generation 36
5.3 Viscous Dissipation 39
5.3.1 Mainstream Dissipation Correlations 42
5.3.2 Boundary Condition Effects 45
6 Quasi-3D Blade Boundary Layer Analysis with MISES 47
6.1 Motivation 47
6.1.1 Case Study Parameters 47
6.1.2 Input Geometries of Select Cases 48
6.2 Boundary Layer Examination 52
6.2.1 CFD vs. MISES 52
6.2.2 Boundary Layer Analysis 54
6.2.3 Linking Boundary Layer Analysis to 3D Loss Trends 56
6.3 Chapter Summary 57

7 Secondary Flow and Losses....58
7.1 Motivation and Set-Up....58
7.2 Secondary Flow Losses and Mitigation....58
7.2.1 Secondary Flow Effects....58
7.2.2 Blade Lean Effects....63
7.2.3 Secondary Flow Loss with Inlet 2....64
7.3 Chapter Summary....66
8 Summary and Future Work....67
8.1 Summary of Redesign and Loss Correlations....67
8.2 Proposed Future Work....68
Appendix A – Turbulence Modelling....69

List of Figures

1-1 Standard Centrifugal Compressor Geometry....11
1-2 Geometric Constraints on Multi-Stage Centrifugal Compressor....12
1-3 Baseline Blade Angle Distribution on (a)Casing and (b)Hub....12

2-1 Meridional Contour of Baseline and Redesigned Impellers....17

3-1 Normalized Entropy (a) Circumferentially-averaged in Meridional View and (b)in Streamwise Planes (View from TE to LE)....21
3-2 Blade loading distribution at 90% Span....22

4-1 Overall Deceleration vs. Change in Loss....25
4-2 Normalized Entropy Contours....26
4-3 Work Input vs. Losses for Different Blading....28
4-4 Work Input vs. Losses (Referenced to Outlet Loss) for Different Blading....28
4-5 Deceleration in Impeller Front vs. Loss....29
4-6 Change in Peak Mach Number (SS) vs. Loss....30
4-7 Three Loss Regions....31
4-8 Normalized Entropy in Major Regions....31
4-9 Mass-averaged Normalized Entropy at Inlet Bend Exit for Different Meshes....32
4-10 Normalized Entropy Distribution at Inlet Bend Exit with Different Meshes with (a)v8 and (b) v82....33

5-1 Normalized Entropy at Inlet Bend Exit....34
5-2 (a) Normalized Stagnation Pressure and (b) Normalized Stagnation Temperature at Inlet Bend Exit....35
5-3 Meridional Curvature of Inlet 1 and 2....36
5-4 Normalized Entropy with Inlet 2....37
5-5 Normalized Entropy contours looking from TE to LE for Inlet 2 Cases....37
5-6 Normalized Entropy at Inlet Bend Exit for two cases with Inlet 1 (v4, v8) and two cases with Inlet 2 (v42, v82)....38
5-7 Passage Length locations for estimation of inlet dissipation....40
5-8 Comparison of Normalized Entropy for v8 based on CFD output and based on dissipation scaling....41
5-9 Coordinate System Definition....41
5-10 Spanwise and Meridional Velocity Definition....42
5-11 Measurement Planes for Inlet 1 and 2....43
5-12 Dissipation Rates at 45°....44
5-13 Dissipation Rates at 90°....44
5-14 Throat Locations for v4 and v8 at Shroud....45
5-15 Normalized Meridional Velocity at Inflow (Boundary Condition)....46

5-16 Normalized Meridional Velocity at 45° for v8.....46

6-1 Blade Geometries at three span locations for MISES Input.....49
6-2 Normalized Streamtube Height for Select Cases.....50
6-3 Normalized Meridional Velocity Vm/Utip.....51
6-4 Relative Mach number at 90% Span.....51
6-5 Relative Mach number for v4 and v8 near LE showing stagnation point moving from PS to SS for reduced incidence.....52
6-6 CFD(Red) vs. MISES(Blue) Blade Loading Distributions at 20% Span.....53
6-7 CFD(Red) vs. MISES(Blue) Blade Loading Distributions at 55% Span.....53
6-8 CFD(Red) vs. MISES(Blue) Blade Loading Distributions at 90% Span.....54
6-9 Boundary Layer Parameters for 90% Span.....55
6-10 Relative Mach number Distribution at 90% Span.....57

7-1 Location of the Leading Edge and Trailing Edge measurement planes in (a) and the normalized entropy in those planes, respectively in (b) and (c).....59
7-2 Secondary flow induced by Passage Vortices (PV), Coriolis Vortices (CV), and Blade Surface Vortices (BV).....60
7-3 Normalized Reduced Pressure on Shroud (Red) and Hub(Blue).....62
7-4 Definitions of Positive and Negative Lean.....63
7-5 Normalized Meridional Velocity Vm/U2 in Wake Region at Trailing Edge.....64
7-6 Spanwise Distribution of Normalized Entropy showing Wake Region at Trailing Edge.....64
7-7 Normalized Meridional Velocity Vm/Utip in Wake Region at Trailing Edge.....65
7-8 Normalized Reduced Pressure on Shroud(Red) and Hub(Blue) for Inlet 2 Cases..65

A-1 Viscosity Ratio at 45° for v4.....70
A-2 Eddy Viscosity Modification Factor at 45° for v4.....71
A-3 Normalized Meridional Velocity at (a)0°, (b)45°, and (c)90° and Normalized Spanwise Velocity at (d)0°, (e)45°, and (f)90°.....72
A-4 Viscosity Ratio at (a)45° and (b)90°.....73

List of Tables

4-1 Blade Angle Distribution Study Cases Examined.....24

6-1 MISES Loss Coefficients.....55

Chapter 1

Introduction

1.1 Background and Motivation

Multi-stage centrifugal compressors are used for a range of applications such as gas injection and oil refining. In these applications, high efficiency and wide operating range are desired. Although there has been much research on centrifugal compressor design, there is still a drive for further improvement of performance.

This thesis examines centrifugal impeller losses, in particular the viscous dissipation inside and outside the boundary layer and secondary flow losses. These losses are linked to changes in the casing blade angle distribution and inlet bend shroud curvature. The results show a potential benefit for a loading distribution with reduced front loading (turning) within the first 20% chord length and reduced inlet bend shroud curvature. An examination of loss mechanisms is also presented.

1.2 Impeller Geometry and Flow Features

Figure 1-1 shows a schematic of the first stage of a multi-stage centrifugal compressor. The stage has an inlet bend, impeller, diffuser, and return channel. The impeller introduces swirl and kinetic energy into the flow. The diffuser and return channel convert the kinetic energy to static pressure rise. The flow then exits the 90° bend and enters the next stage, ideally with no swirl. Return channel features, including the return bend, return vane, and 90° bend, were examined in previous studies [1, 2]. Computational results at the impeller exit were used as the inlet boundary condition for the return channel studies. The focus of the current study is the inlet and shrouded impeller. Leakage flow is not included in the computations.

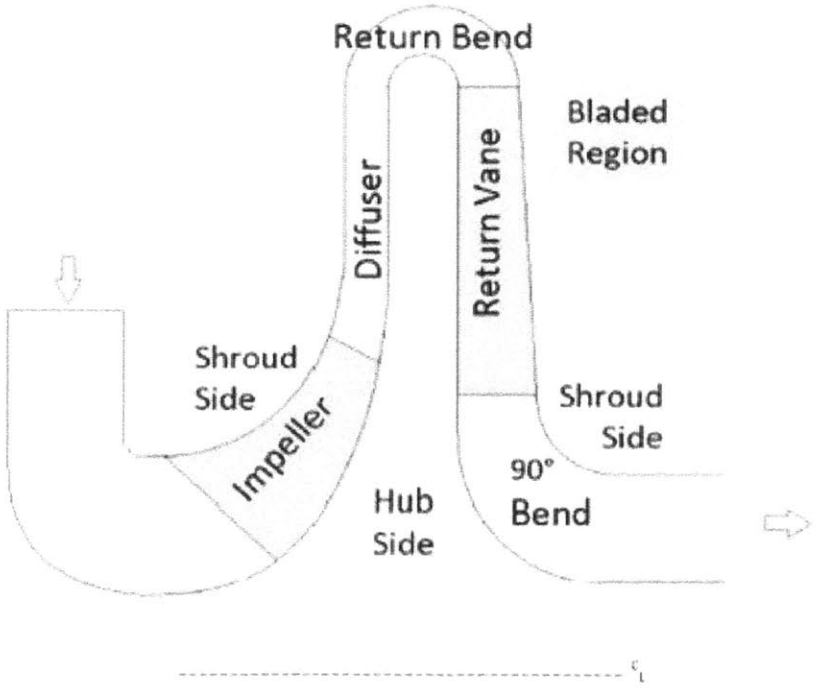

Figure 1-1: Standard Centrifugal Compressor Geometry

Figure 1-2 shows a schematic meridional view of the geometric constraints for a centrifugal compressor. These include maximum diameter, axial stage length, hub and tip diameter of return channel exit, inlet flow path, and impeller meridional curvature. In this

study, the leading edge and trailing edge meridional location as well as the hub and shroud locations of the shrouded impeller were unchanged.

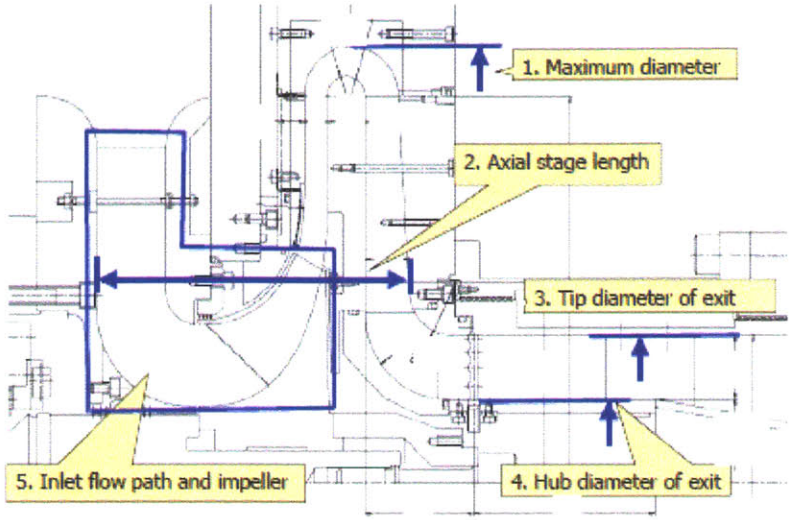

Figure 1-2: Geometric Constraints on Multi Stage Centrifugal Compressor

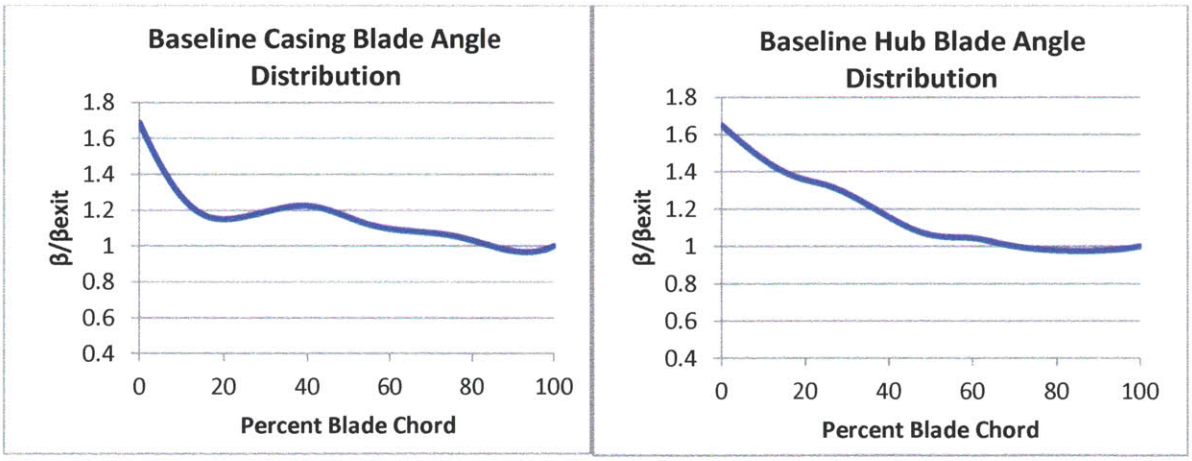

Figure 1-3: Baseline Blade Angle Distribution on (a)Casing and (b)Hub

Figure 1-3 shows blade angle distributions on the casing and hub for a representative impeller[1]. At each span, the angle shown is the blade metal angle at the centerline of the blade normalized by the trailing edge metal angle. The 3D blade geometry is defined by linearly connecting the hub and casing blade angle distributions.

[1] Provided by A. Nakaniwa, 2011.

The impeller has high efficiency, and the present work examines possible areas of further improvement.

1.3 Nomenclature

The term "passage length," which is referred to subsequently, is a normalized meridional coordinate that is 0% at the inlet bend exit (i.e. beginning of the shrouded impeller) and 100% at the outlet of the shrouded impeller. Other relevant locations, such as the 20% passage length location, will be defined in the text. We also refer to PS (pressure side), SS (suction side), LE (leading edge), and TE (trailing edge). All variables are defined in the text.

1.4 Previous Work

For axial compressors, it has been shown that prescribed velocity distribution (PVD) or controlled diffusion (CD) airfoils can improve peak efficiency and flow range [3]. Features of PVD design recommendations include [4]:

- Rapid acceleration near the leading edge, on the suction side, up to a Mach number of about 1.3
- A steep initial deceleration region which relaxes toward the trailing edge
- A constant pressure side subsonic Mach number

Sieverding [3] has described these guidelines. The highest efficiency airfoil he examined had the location of maximum blade thickness at about 25% blade chord (compared to 40% blade chord for NACA65 airfoil). High turning in the front region of the blade led to a peak Mach number on the suction side near 5% blade chord, followed by a deceleration to 30% blade chord. The intent is to turn the flow while the boundary layer is thin, and the deceleration lessens for the latter part of the blade to prevent separation.

Calvert and Ginder [5] examined the validity of this recommendation for transonic axial compressors. They provided further experimental support for the design guidelines,

noting that rear loading typically leads to separation. For high subsonic flow, their studies show there is a benefit of low turning in the front 30% blade chord to promote reattachment after the leading edge. They also limit the peak Mach number to about 1.3, as highlighted by Walraevens [4].

Zangeneh [6] and Hiradate [7] proposed guidelines for centrifugal compressor impellers. Zangeneh suggests inclining the blades linearly against the direction of impeller rotation (i.e. blade at the hub leads the blade at the shroud in the direction of rotation) to suppress secondary flows and reduce overall loss. Hiradate noted that although this design suppressed secondary flows, it increased the pressure on the suction shroud side and decreased the velocity near the throat, moving the stall point to a higher flow rate. Inclining the blades against the direction of impeller rotation also promoted an accumulation of loss in the suction hub corner. Hiradate suggested a curvilinear blade stacking, as well as a reduction of turning up to the throat near the casing. Reducing turning improved the stall margin, and the curvilinear negative lean maintains the suppression of secondary flow [7].

1.5 Research Questions

In this thesis, the following research questions are addressed:

(1) Can modifications to the blade angle distribution improve impeller performance?

(2) What are the links between blade angle distributions and loss production?

(3) Are there design features that should be examined to show potential for improving overall efficiency?

1.6 Thesis Contributions

(1) The losses for the first stage impeller of a multi-stage centrifugal compressor are characterized. The effect of these mechanisms on flow structure and overall loss has been evaluated using quasi-3D boundary layer and 3D RANS calculations.

(2) Modifications that reduced the overall loss are described. These modifications include a casing blade angle distribution with roughly 60% of total casing blade angle change in the front 20% blade chord and a negative lean (as permitted by structural limitations) to mitigate the loss sources determined in (1).

Chapter 2

Implementation

2.1 Computational Approach

2.1.1 ANSYS CFX

Numerical simulations of the 3D impeller flow were performed using the commercially available ANSYS CFX code Version 14.5. The computational domain included a stationary inlet, a rotating shrouded impeller, and a vaneless diffuser, as sketched in Figure 2-1. The radially-extended pinched diffuser is added to aid in solver convergence[2]. Frozen rotor interfaces were imposed between the stationary and rotating domains. These interfaces fix the relative position between the domains during computation and apply the appropriate frame transformations at the interface[3]. Mixing planes were not used. Three dimensional calculations were performed for a single passage, with periodic boundary conditions. Second order discretization was used for all calculations.

The turbulence model employed was the $k-\omega$ SST model, used in previous work on a return channel redesign [1,2]. A turbulence intensity of 5%, as used in previous work, was specified [1,2]. The SST model is used because of its increased correlation with boundary layer data in adverse pressure gradient flows [8] compared to other two-equation eddy viscosity models. This feature is related to accounting for transport of turbulent shear stress. The SST model is also preferred for its fast computation time in comparison with more complex RSM (Reynolds Stress) turbulence models [8]. The SST

[2] Personal communication with Dr. C. Lettieri, 2012
[3] FLUENT v14 Documentation, Section 5.3.3.1.2

model can resolve the boundary layer with a coarse mesh [9] with the use of wall functions.

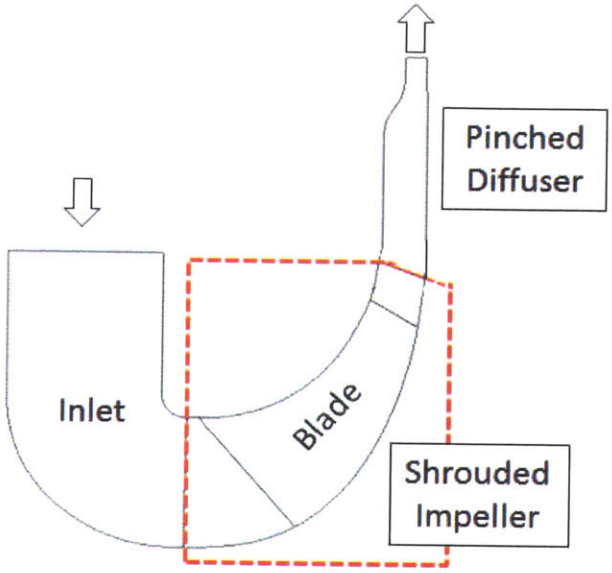

Figure 2-1: Meridional Contour of Baseline and Redesigned Impellers

The SST model is a combination of the $k-\epsilon$ and $k-\omega$ two-equation models with a blending function to link them. The $k-\omega$ model produces more realistic boundary layer behavior than $k-\epsilon$ in adverse pressure gradients [10]. The $k-\epsilon$ model produces more realistic free stream flow profiles and turbulence properties than $k-\omega$ but can overestimate the shear stress in adverse pressure gradients due to underestimation of the turbulent eddy dissipation [10]. To obtain the advantages of both models, SST uses $k-\epsilon$ in the free stream and converts to $k-\omega$ with the use of a blending function.

The SST model also assumes turbulence isotropy, which allows the Reynolds stresses to be approximated by using mean flow quantities. Because of this approximation, SST is known to deviate from experimental data for flows with sudden changes in mean strain rate, for example flows with streamline curvature of 90° or higher [9]. The known accuracy of the model is based on agreements with experimental data on boundary layers

and backward-facing step flow [10], and the model is widely used in industrial analyses of turbomachinery[4].

2.1.2 MISES

MISES (Multiple blade Interacting Streamtube Euler Solver) is a quasi-3D solver that uses integral boundary layer equations in an interactive inviscid freestream - viscous boundary layer analysis[5]. MISES was used to analyze the blade boundary layers at different span locations. The MISES solutions do not incorporate the influence of the crossflow. Based on the loss trends for different impellers (as seen in Chapter 4), MISES is a useful tool for determining boundary layer parameters in regions of small crossflow and thus for determining the effect of blade geometry on losses.

2.2 Mesh Generation

All impellers for the ANSYS CFX calculations were created in BladeGen, where meridional contours, blade angle distributions at the casing and hub, and blade thicknesses were specified. Defined impellers were then imported to TurboGrid and meshed using the automatic meshing feature. The impeller, inlet bend, and extended diffuser were meshed separately, using the "Inlet/Outlet Domain" feature to minimize high aspect ratio elements in the passage. Mesh size was approximately 800,000 grid points for all impellers.

2.3 Boundary Conditions

The CFX calculations were performed on a single passage of the baseline and redesigned impellers, all of which contained 13 blades. Inlet conditions were standard temperature and pressure. The passage mass flow was specified. Where convergence issues occurred, static pressure was specified at the outlet to achieve a mass flow within +/-1% of the design mass flow. The impeller tip Mach number is 0.97.

[4] FLUENT v14 Documentation, Section 2.2.2.6
[5] MISES documentation 2.6.7

2.4 Performance Metrics

The metric for evaluating the impeller losses is:

$$\zeta = \frac{T_{tinlet} * (s - s_{inlet})}{U_2^2}$$

where U_2 is the tip speed, T_{tinlet} is the stagnation temperature at the inlet, and s is the calculated entropy. The above quantity will be referred to as the normalized entropy. The stage operating condition is determined by the flow coefficient, defined as in previous work [2] as:

$$\varphi = \frac{\dot{m}}{\rho_{tinlet} U_2 \frac{\pi}{4} D_2^2}$$

where $\dot{m}$ is the total impeller mass flow, ρ_{tinlet} is the stagnation density at the inlet, and D_2 is the average trailing edge diameter. The isentropic efficiency is defined as:

$$\eta_s = \frac{PR^{\frac{\gamma-1}{\gamma}} - 1}{TR - 1}$$

where PR is the total-to-total pressure ratio and TR is the total-to-total temperature ratio between the inlet and a defined plane after the impeller exit. In consistency with previous work, the plane was taken as 20% of the impeller exit width downstream, in order to not have reverse flow at design.

Chapter 3

Characteristics of Baseline Impeller Flow

3.1 Loss Production in Impeller

Figure 3-1 shows normalized entropy contours for the baseline impeller in a circumferentially mass-averaged meridional view and also at different meridional locations along the flow path. There is appreciable loss in the inlet bend near the shroud and on the blade surfaces although there was no separation. The meridional curvature creates a positive pressure gradient from the shroud to the hub, and the higher velocities on the shroud lead to higher losses on the shroud than on the hub[6].

The contours along the flow path show the migration of loss toward the suction side shroud corner, indicating secondary flow due to pressure gradients from meridional and blade curvatures. The influence of secondary flow on the production of loss will be discussed subsequently.

It is known that the casing blade angle distribution, as shown in Figure 1-3(a), is more influential on impeller performance than the hub blade angle distribution [11] due to higher velocities near the casing and accumulation of loss on the casing from secondary flow. Figure 3-2 shows the static pressure distribution at 90% span, defined by the static pressure coefficient as:

$$Cp = \frac{\overline{P_{trel_{upstream}}} - P}{\overline{P_{trel_{upstream}}} - \bar{P}_{upstream}}$$

[6] The boundary layer loss scales approximately as the cube of velocity [26].

where P_{trel} is the relative stagnation pressure, P is the static pressure, and the upstream quantities are mass-flow averaged over the circumferential direction:

$$\bar{x} = \frac{\sum \dot{m}_n x_n}{\sum \dot{m}_n}$$

The upper curve of the blade loading diagram represents the pressure surface, and the lower curve represents the suction surface. The spikes near normalized blade chord ≈0 in Figure 3-2 are indications of incidence, and thus loss [12], as flow moves around the leading edge. Changes to the inlet blade metal angle to help reduce this loss will be described in Chapter 4. Near 10% blade chord, on the suction side, the flow begins to decelerate steadily with a more rapid diffusion taking place at the rear of the blade. We will investigate the benefits of different blade angle distributions.

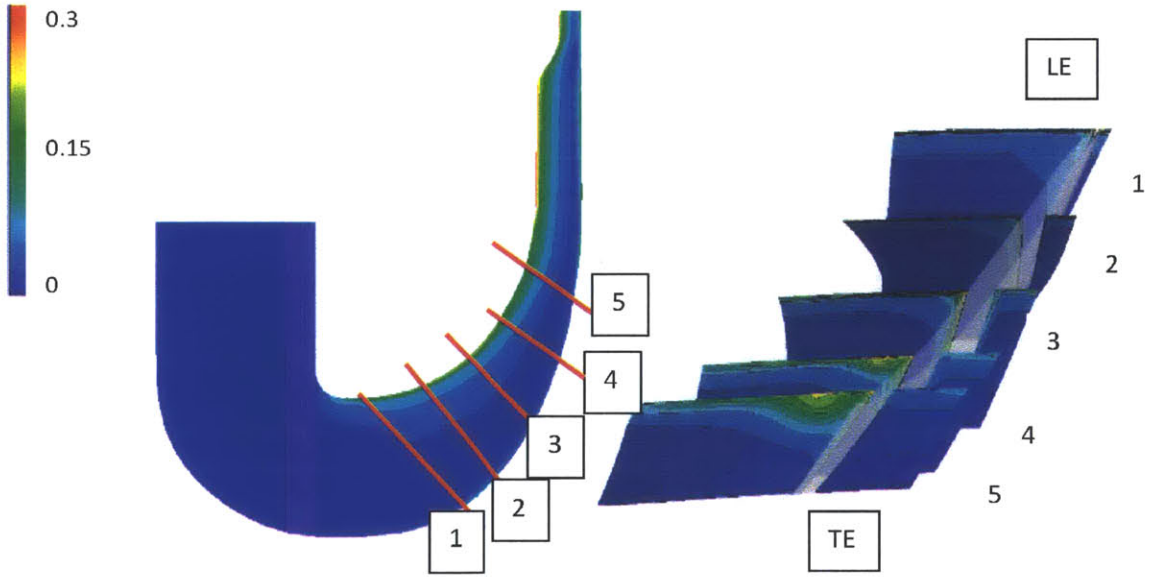

Figure 3-1: Normalized Entropy (a) Circumferentially-averaged in Meridional View and (b)in Streamwise Planes (View from TE to LE)

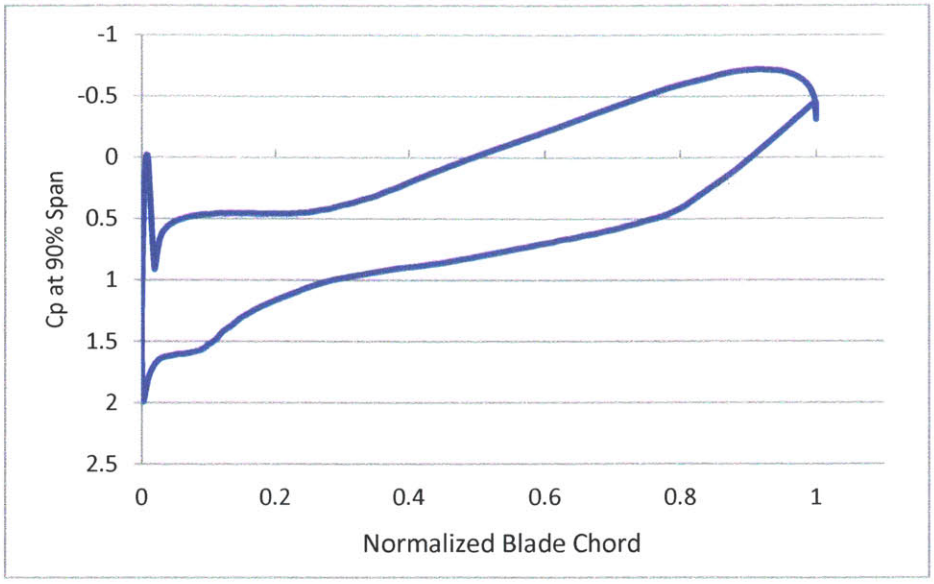

Figure 3-2: Blade loading distribution at 90% Span

Chapter 4

Blade Geometry Assessment

4.1 Case Study Motivation and Parameters

The goal of the present study is to define the links between blade angle distributions (as prescribed at the hub and shroud) and the losses for a series of impellers covering a spectrum of blade angle distributions. The losses will be correlated to given blade angle changes, or flow turning.

The casing blade angle distribution is typically more influential on compressor performance than the hub distribution [11], and the study focuses on modifying the former. To keep flow capacity the same, the hub blade angle distribution was modified so the cross-sectional throat area is within +/-5% of the baseline throat area (ANSYS BladeGen outputs the throat area, and the hub blade angle distributions were modified until an acceptable throat area was achieved). The trailing edge blade angles were kept the same. The result was that the computations converged with a mass flow within +/-1% and a work input within +/-1% of the baseline work input. The blade thickness distribution, specified at the hub and shroud, was kept the same for all cases (The blade angle and thickness distributions are specified at the hub and shroud, and the blade geometry is created by linearly connecting these distributions).

4.2 Blading Examined

Table 4-1 shows the blading examined. As stated, the focus was the casing blade angle distribution. The leading edge angle is defined in reference to β_{ref}, which is the baseline leading edge angle on the casing. The impellers are categorized by the percent of turning in this front 20% blade chord[7], or *front turning*. v0 is the baseline design. The first redesign, v1, smooths the blade angle distribution. v2 is more flattened and with slightly less front turning (61%) than v1. v4 has high front loading, with 80% turning in the blade front region. v5 has reduced incidence on the casing and a reduced front turning (73%) compared to the baseline. v5c has a slightly reduced front turning (70%) compared to v5 and reduced incidence on both the hub and casing. v8 has the least front turning of all cases and reduced incidence on the hub and casing, with 60% front turning.

Case	Description	% Turning in Casing Front	LE $\beta - \beta_{ref}$, Casing (Degrees)
v0	Baseline	79	0
v1	Smooth variation than v0	63	0
v2	Flatten v1	61	0
v4	High front turning	80	0
v5	Reduce v4 turning and incidence on casing	73	5
v5c	Similar to v5 with reduced incidence on casing and hub	70	5
v8	Low front turning (red. incid. on casing+hub)	60	5

Table 4-1: Blade Angle Distribution Cases Examined

[7] Recommendation of Dr. M. Casey (May 2014). Note: Other percent blade chord could have been used(i.e. 25%, 30%, etc) to categorize the impellers. This is not to be confused with the percent blade chord location that will be shown to be most relevant to the losses, which is 10% blade chord.

4.3 Loss Production Correlations with Blading

4.3.1 Overall Loss Trends

A way to characterize impeller diffusion is the deHaller number, which represents a measure of the overall deceleration within a rotor. The deHaller number is:

$$deHaller\ number = \frac{\overline{W2}}{W1_{max}}$$

where $\overline{W2}$ is the relative velocity at the impeller exit plane and $W1_{max}$ is the maximum relative velocity at the inlet exit (start of shrouded impeller). Figure 4-1 shows the deHaller number plotted against change in loss coefficient compared to the baseline, v0 (at the 0% horizontal line). The loss coefficient, defined in Section 2.4, is based on the total loss generated up to the impeller exit plane. All cases had loss equal to the baseline or less, except for v4, the highly loaded case. The trend is that as the deHaller number increases, and the overall deceleration decreases, the loss reduces. The case with least loss, v8, has an 8% loss reduction compared to the baseline. Reducing incidence also reduces overall loss.

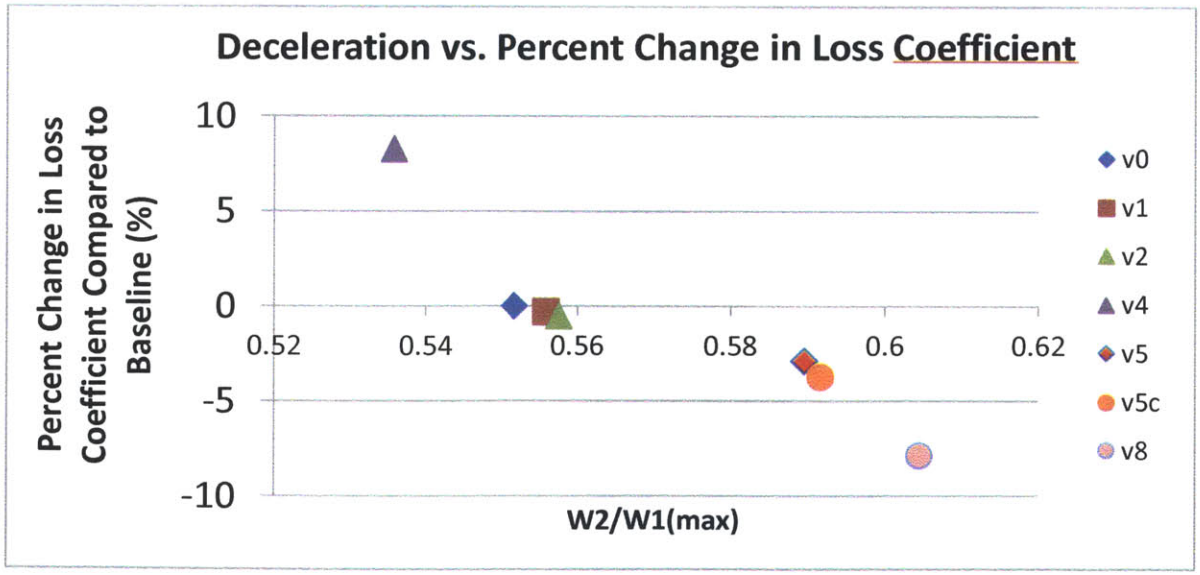

Figure 4-1: Overall Deceleration vs. Change in Loss

Impellers v0, v1, v2, and v4 have the same incidence. For these impellers, reducing the overall deceleration reduced loss. For the cases with reduced incidence, v5, v5c, and v8, a trend of reduced overall deceleration reducing losses is also shown. This is interesting because axial compressor guidelines recommend higher front turning to have the turning take place while the boundary layer is still thin [3].

Figure 4-2 shows normalized entropy contours for three cases: v4 (high front turning), v5c (high front turning and lower losses than the baseline), and v8 (low front turning and least loss). The loss development along the suction side – shroud corner can be seen. The region of loss moves from the suction side surface toward the casing along the flow path, such that the low energy, high loss region at the trailing edge is thin on the blade and thicker on the shroud.

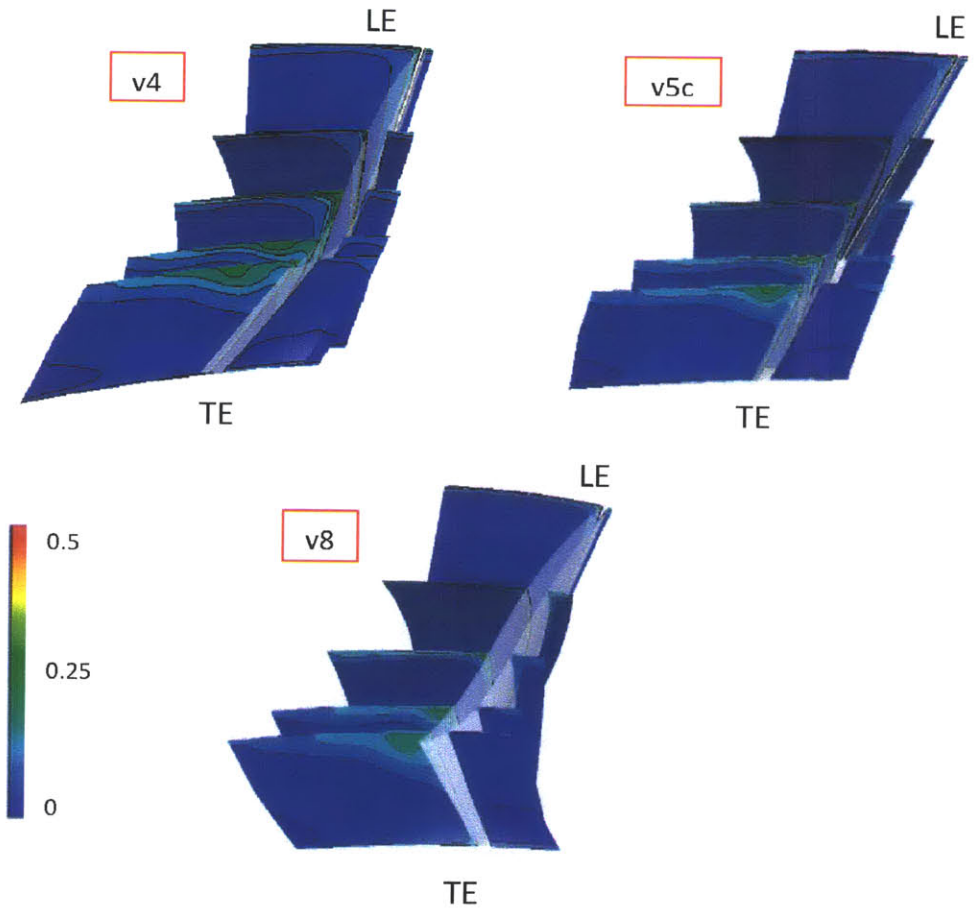

Figure 4-2: Normalized Entropy Contours

The movement of loss indicates the presence of secondary flow, but it is not clear whether the secondary flow is a source of loss or rather a transporter of high entropy flow to a new location. We thus investigate the flow in more depth to determine the source of the loss generation region.

4.3.2 Locating Loss Generation Regions

Figure 4-3 shows normalized mass-averaged entropy vs. normalized mass-averaged stagnation enthalpy, λ:

$$\lambda = \frac{(\overline{h_t} - \overline{h_{t,inlet}})}{U_2^2}$$

The normalized stagnation enthalpy and normalized entropy are at cross-sectional planes along the flow path for each case. All the cases have entropy production before the leading edge, from both mainstream and boundary layer dissipation, as will be discussed in Chapter 5. The stagnation enthalpy begins to rise after the leading edge, and after about 20% passage length, all cases have a similar change in entropy per unit work input. In Figure 4-4, the curves are overlaid and referenced to the normalized entropy in the impeller exit plane, showing that the main difference in the loss production occurs before the 0.1 normalized stagnation enthalpy line, or roughly by 20% passage length into the impeller.

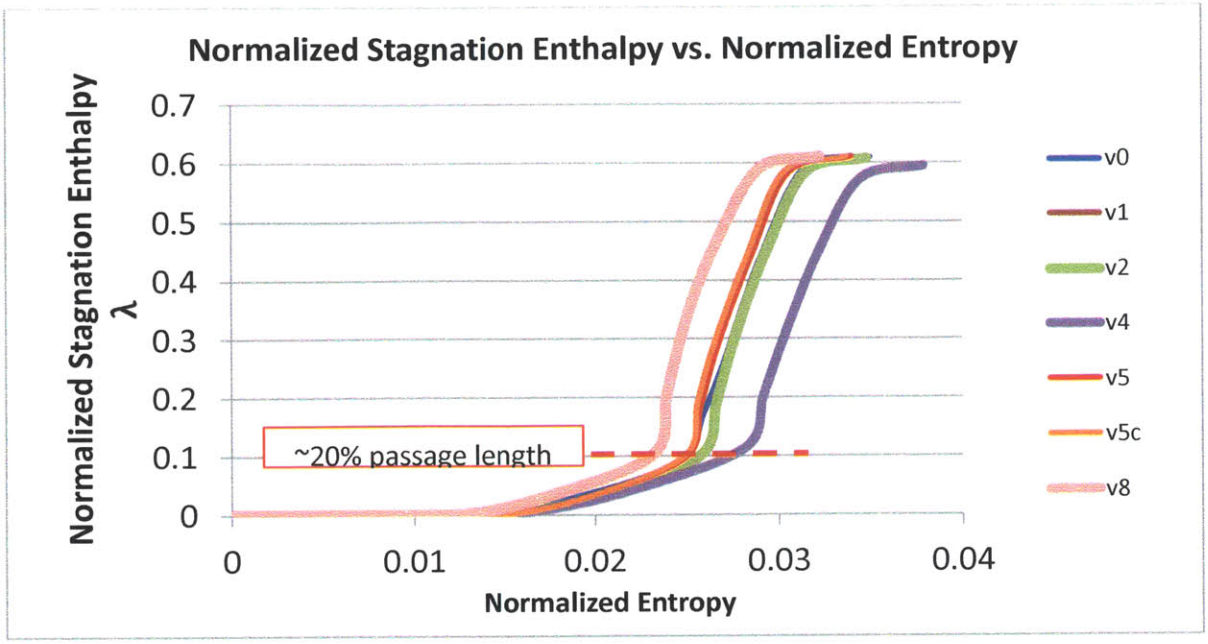

Figure 4-3: Work Input vs. Losses for Different Blading

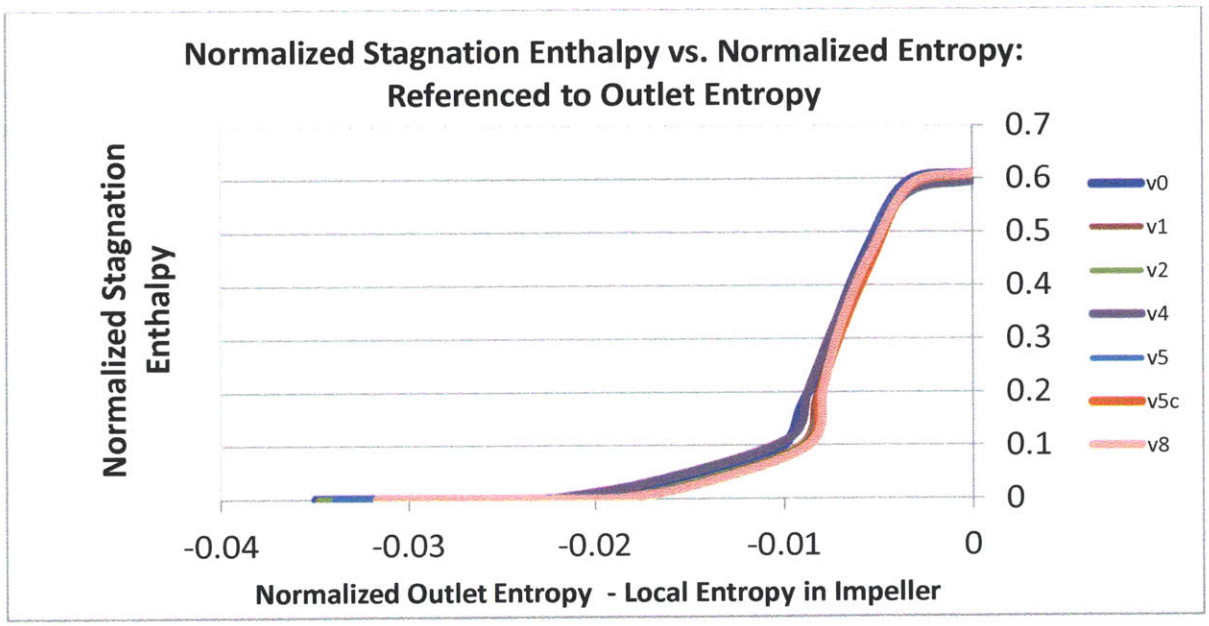

Figure 4-4: Work Input vs. Losses (Referenced to Outlet Loss) for Different Blading

4.3.3 Local Loss Trends

Figure 4-3 and 4-4 imply that much of the loss production is in the front 20% of the passage length. In this context, Figure 4-5 shows the deceleration between the start of

the shrouded impeller and the 20% passage length plane. As in the overall loss trends of Figure 4-1, an increase in $\frac{\overline{W_{20\%}}}{W_{1,avg}}$, corresponding to less deceleration in the front region of the blade, is associated with decreased loss. The reduced deceleration in the front region of the blade corresponds to a reduced peak relative Mach number on the suction side, as in Figure 4-6. Making this comparison at other passage length locations (30%, 40%, etc.) does not show trends in deceleration that correspond to the overall loss trend, implying a link between the blade geometry up to the 20% passage length location and overall losses. Figures 4-5 and 4-6 thus suggest a connection with deceleration in the front region of the blade, up to 20% passage length, and the behavior of the blade boundary layer. It is difficult to extract the boundary layer parameters from these computations and pinpoint the link between the flow field, the loss, and the blade geometry, and boundary layer computations to be discussed in Chapter 6 were thus performed to help define this link.

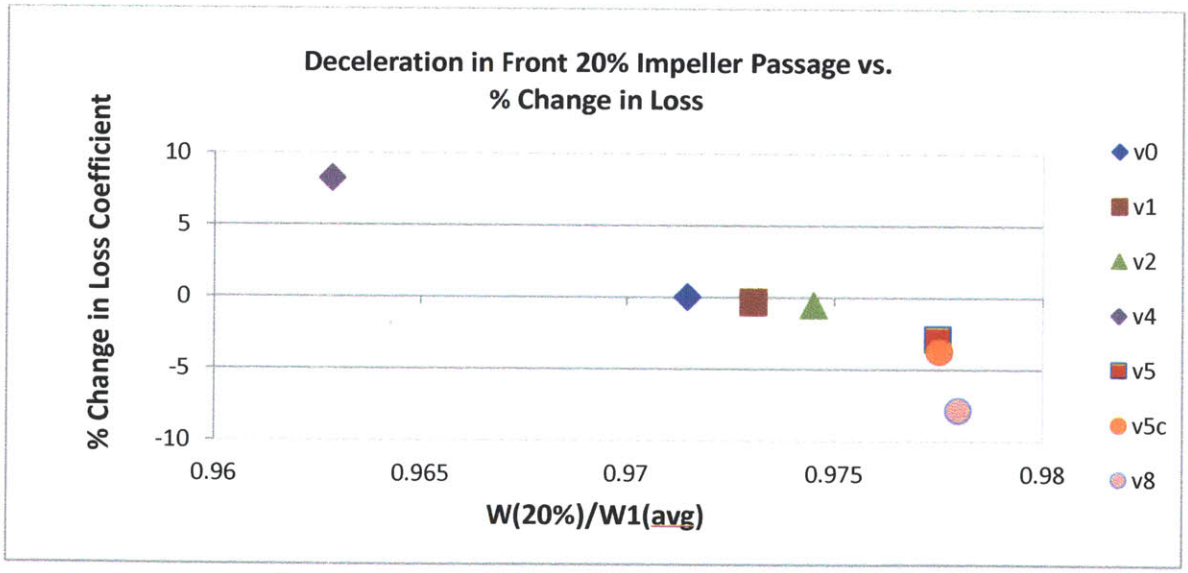

Figure 4-5: Deceleration in Impeller Front vs. Loss

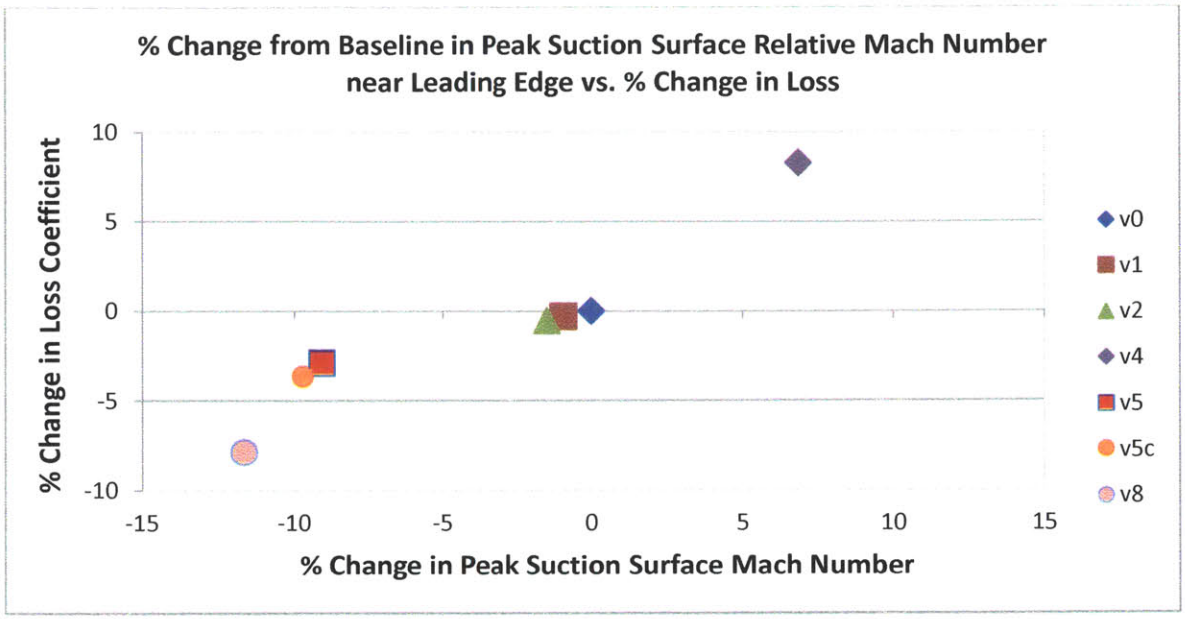

Figure 4-6: Change in Peak Mach Number (SS) vs. Loss

The inlet loss was found to be appreciable; see the discussion in Chapter 5. It is thus useful to separate the loss developed in the inlet from the losses in the impeller and to divide the flow domain into three major regions: inlet loss, inlet exit to 20% passage length loss, and post-20% loss. Figure 4-7 gives a sketch of these regions, and Figure 4-8 shows the contributions to the overall losses for each. The inlet loss for both v4 and v5c are similar, within .4%, and the v8 inlet loss is 18% less than the other cases. Between the inlet exit and 20% passage length, v4 has the most loss, and v8 has the least loss with the losses correlating with the deceleration in this region (Figure 4-5). In the post-20% region, v5c has the lowest loss, and v4 has the highest loss.

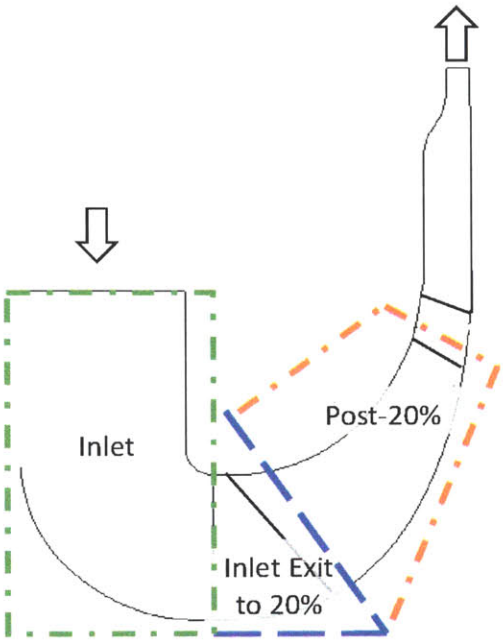

Figure 4-7: Three Loss Regions

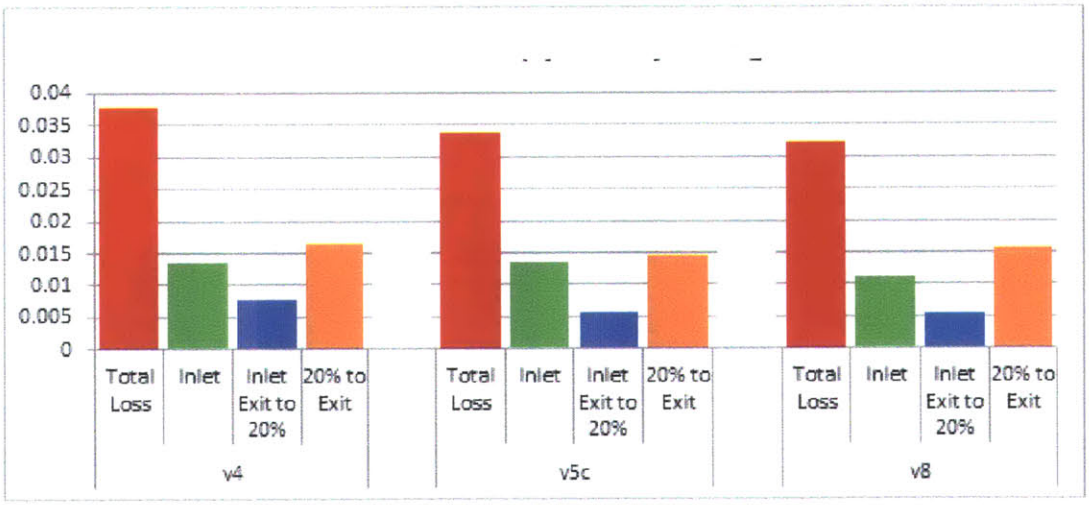

Figure 4-8: Normalized Entropy in Major Regions

4.4 Mesh Refinement Analysis

It was seen in the previous section that the computed inlet loss represented 35-40% of the overall losses. There was a concern that this result was not an appropriate representation of the physical situation. A mesh refinement analysis was therefore performed

on v8 and v82 (case with v8 impeller and reduced shroud inlet curvature - See Chapter 5). The original mesh for v8 had y+ values of 80 in the region of the inlet bend with high curvature. Two other meshes with a y+ of 30 and of 10 in this region were examined. Meshes with y+ of 80 (original) and 10 (fine grid) were examined for v82. Figure 4-9 shows the mass-averaged entropy rise in the inlet bend for these cases. Reducing y+ decreased the inlet loss by 40% for v8 and by 6% for v82. Figure 4-10 (a) and (b) show the normalized entropy distribution at the inlet bend exit for these cases.

Due to time constraints, further analysis on the refined meshes was not performed, and the computations described in the following chapters were carried out on the original meshes. In terms of differences seen, the velocity profiles at the inlet bend exit are changed by less than 0.1%, and the 2D calculations in Chapter 6 are not unaffected. The overall entropy rise at the impeller exit shown in Chapter 7 will be reduced.

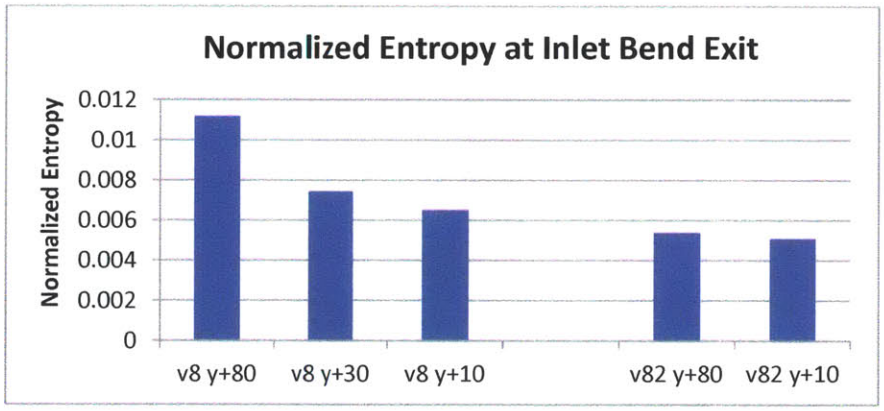

Figure 4-9: Mass-Averaged Normalized Entropy at Inlet Bend Exit for Different Meshes

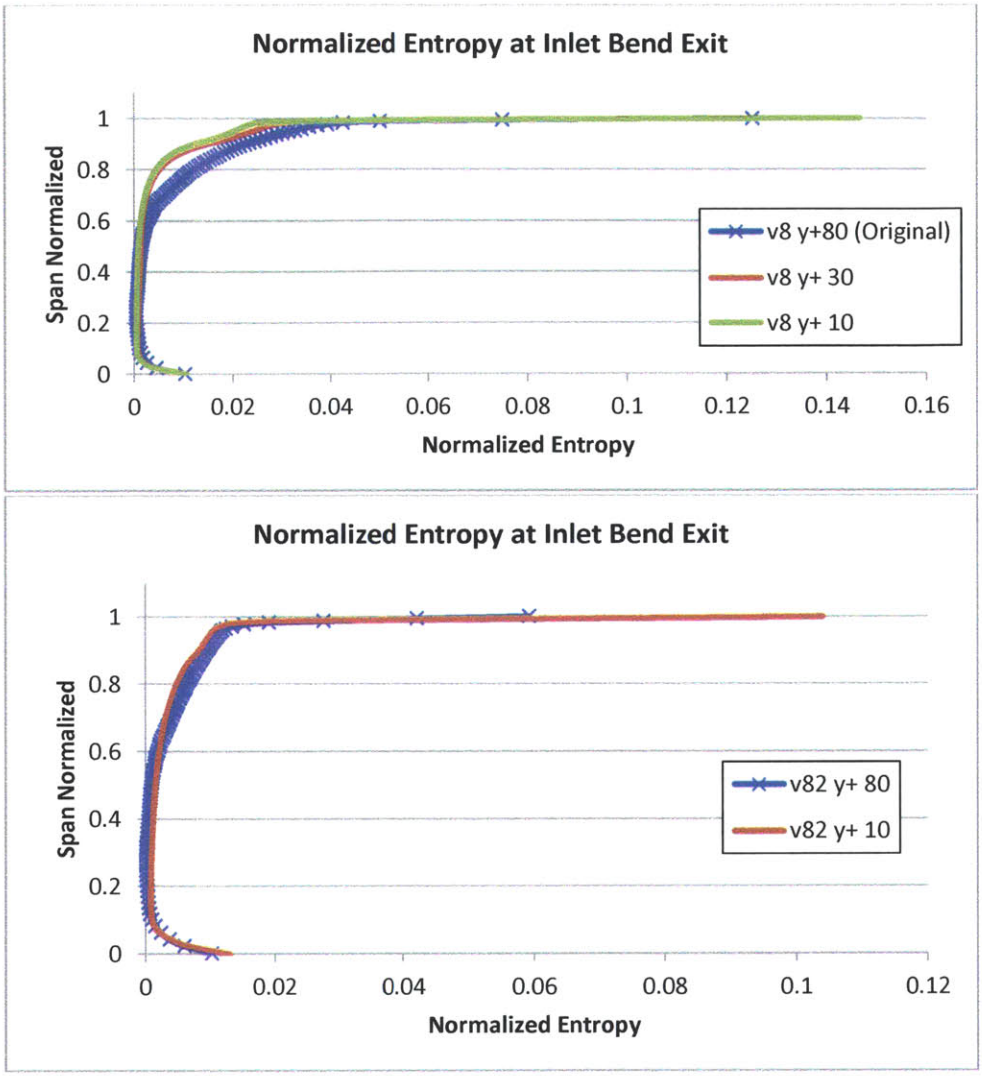

Figure 4-10: Normalized Entropy Distribution at Inlet Bend Exit with Different Meshes with (a) v8 and (b) v82

4.4 Chapter Summary

Three loss regions have been identified: inlet, inlet exit to 20% passage length, and post-20% passage length to the impeller exit plane. For a given incidence, reduced front loading was found to lead to reduced overall losses. The inlet exit to 20% passage length location has loss trends with reduced deceleration. The growth in loss is similar for all impellers after the 20% passage length location. In Chapters 5, 6, and 7, the different loss regions and the loss mechanisms will be described.

Chapter 5

Inlet Dissipation

5.1 Motivation

Figure 5-1 shows the normalized entropy distribution at the inlet bend exit for the three impellers v4, v5c, and v8. All cases have appreciable entropy rise above 60% span. The mass-averaged entropy rise in the bend for v8 is 18% lower than that for v4.

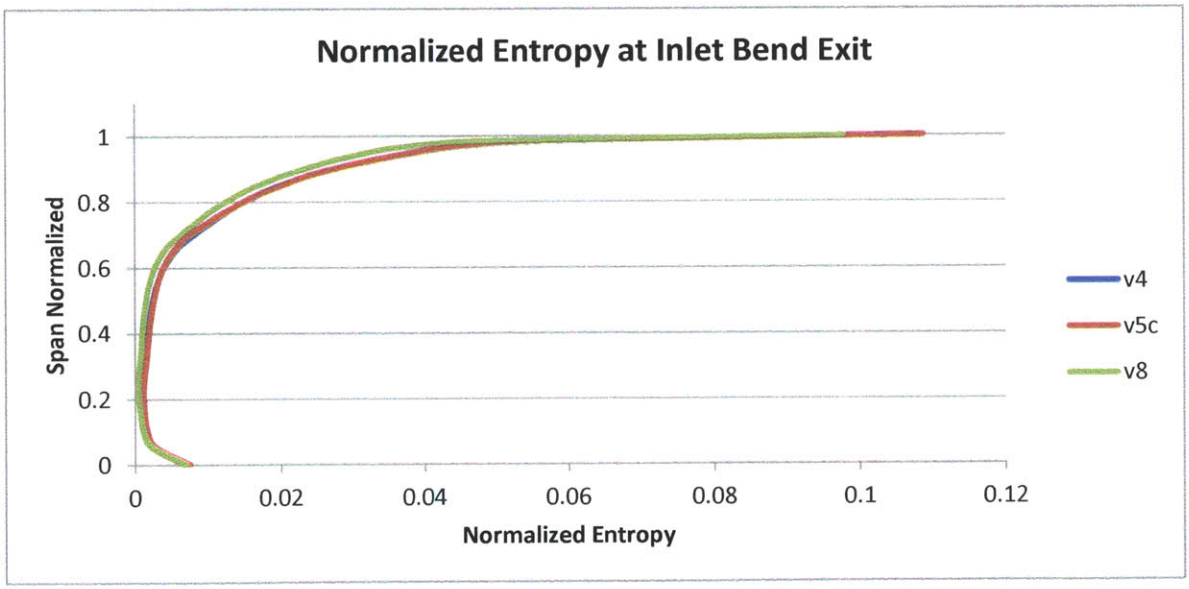

Figure 5-1: Normalized Entropy at Inlet Bend Exit

All cases exhibit viscous dissipation outside the boundary layer, above roughly 60% span. Figure 5-2 (a) and (b) show the normalized stagnation pressure and stagnation

temperature, $\frac{P_t}{P_{tinlet}}$ and $\frac{T_t}{T_{tinlet}}$, at the inlet bend exit. For an ideal gas with constant C_p, the entropy rise is:

$$\Delta s = s - s_{ref} = C_p \log\left(\frac{T_t}{T_{tref}}\right) - Rlog\left(\frac{P_t}{P_{tref}}\right)$$

The reference position chosen for these calculations is the start of the inlet. Figure 5-2 (a) and (b) verify that the entropy change arises from total pressure changes.

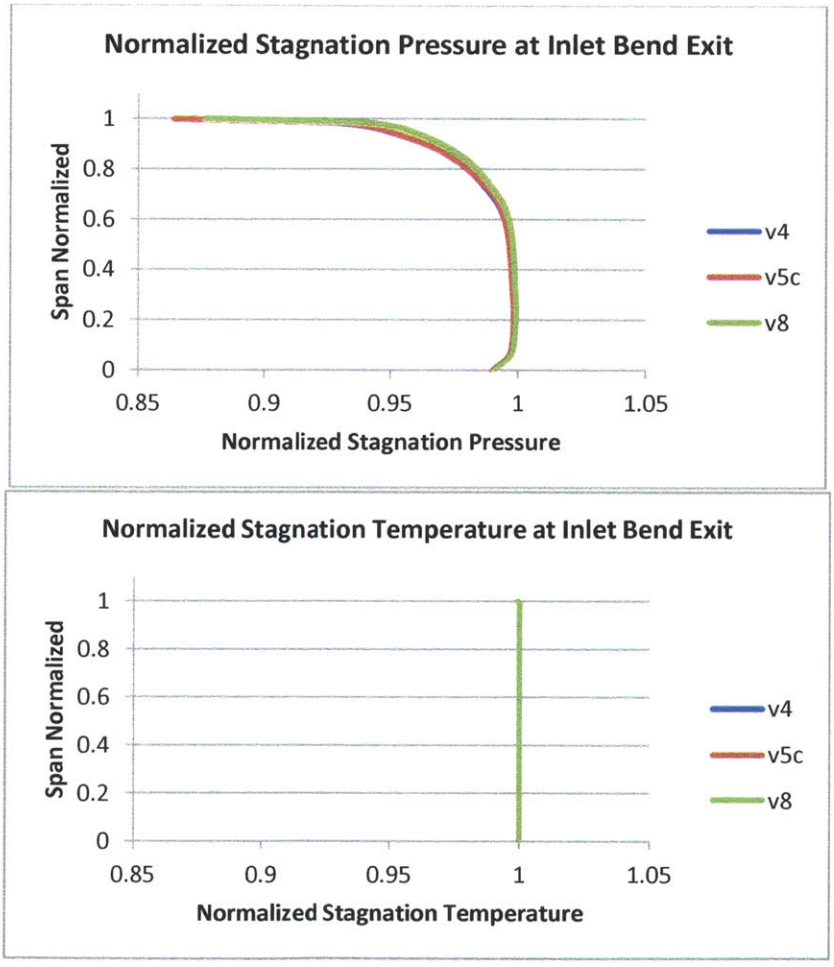

Figure 5-2: (a) Normalized Stagnation Pressure and (b) Normalized Stagnation Temperature at Inlet Bend Exit

5.2 Effect of Inlet Shape

To assess the influence of the inlet geometry on the computed entropy rise, a further MHI design was examined. This second geometry has a 30% reduction in inlet width, as in Figure 5-3, and thus an increased radius of curvature on the shroud.

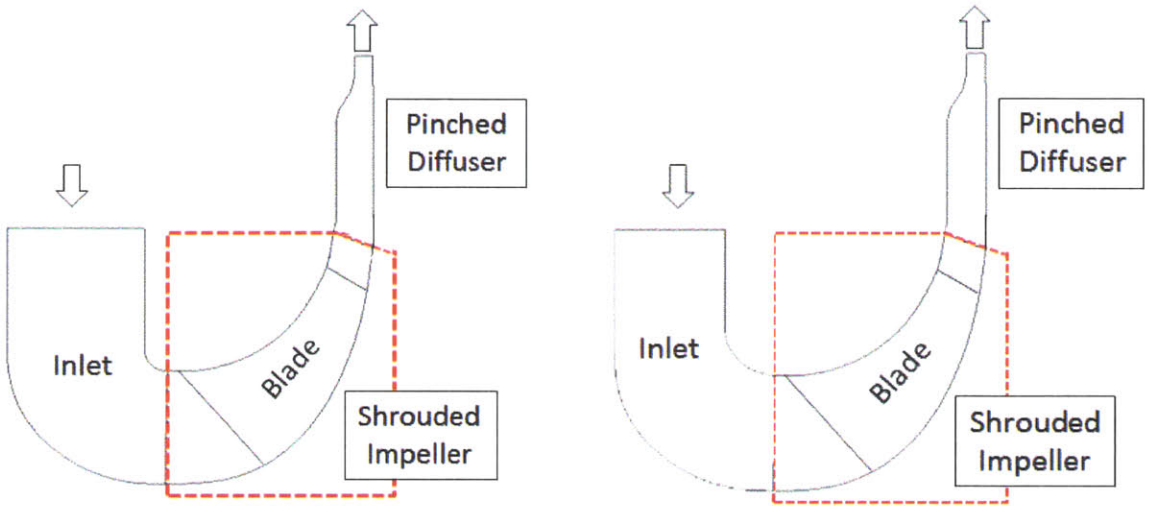

Figure 5-3: Meridional Curvature of Inlet 1 and 2

5.2.1 New Inlet Entropy Generation

Figure 5-4 shows the contribution to the total entropy in the three regions discussed in Chapter 4: (i) inlet bend, (ii) inlet bend exit to 20% passage length, and (iii) post-20% passage length. The cases with reduced inlet width (inlet 2) will be referred to as v42, v5c2, and v82 for the v4, v5c, and v8 impellers, respectively. All cases have a reduction in overall loss compared to that for the original inlet: 14% for v42, 13% for v5c2, and 24% for v82. The loss in the inlet bend for v42 and v5c2 is reduced by 30%, while the inlet bend loss increase for v82 is reduced by 50%.

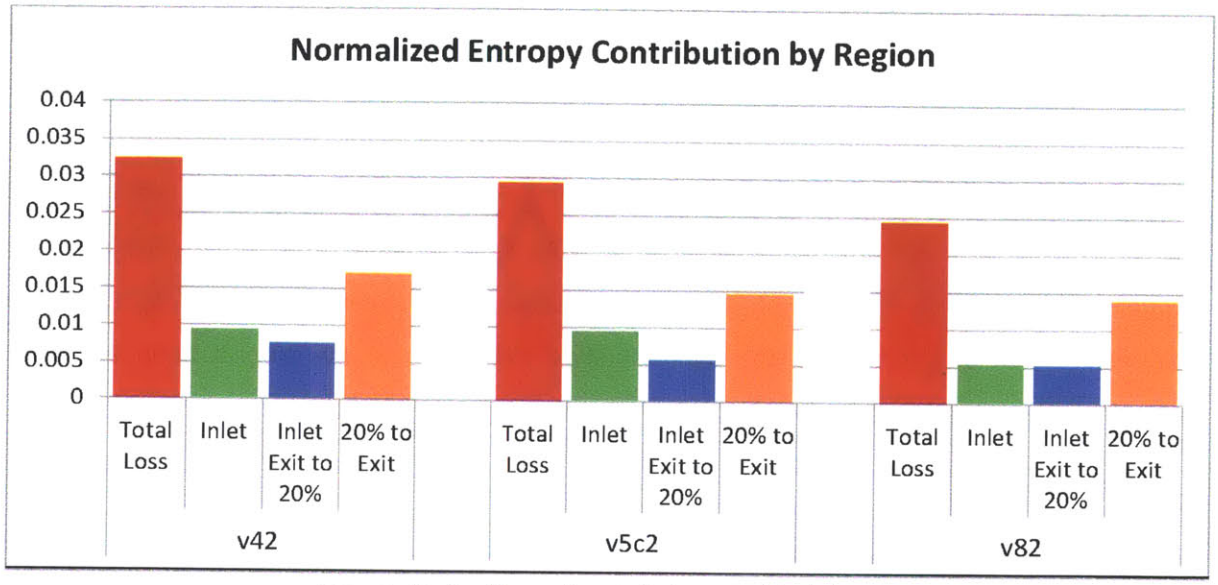

Figure 5-4: Normalized Entropy with Inlet 2

Figure 5-5 shows normalized entropy contours along the blade at the meridional locations in Figure 4-3 for cases v42, v5c2, and v82. All cases show reduced high entropy regions on the shroud and suction side at the leading edge compared to the cases with inlet 1.

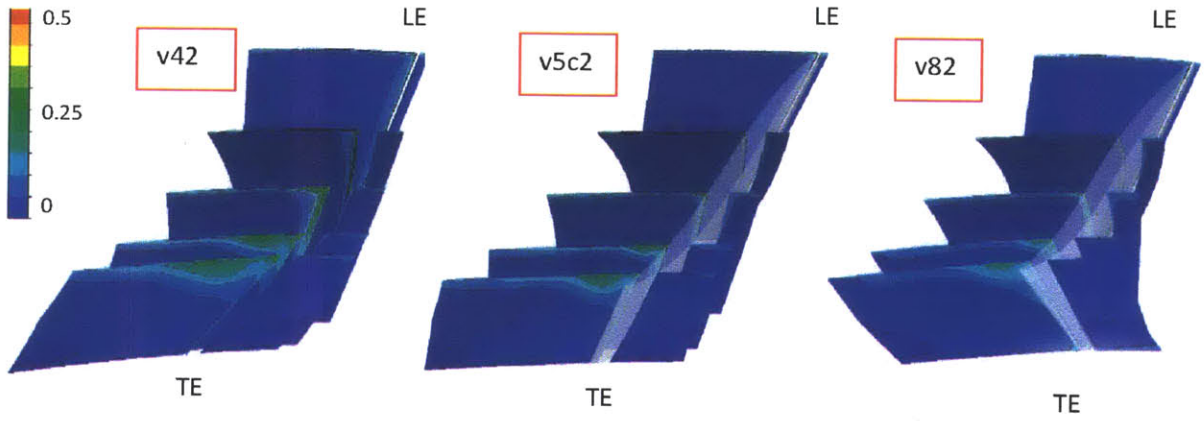

Figure 5-5: Normalized Entropy contours looking from TE to LE for Inlet 2 cases

Figure 5-6 shows the normalized entropy at the inlet bend exit for v4 and v8, with inlet 1, and v42 and v82, with inlet 2. The boundary layer loss at the shroud is reduced by using a reduced front loading. Comparing cases with the same blade distribution, cases v4 and v42 have a similar entropy distribution up to about 60% span. Cases v8 and v82 also have a similar entropy distribution up to about 60% span. From 60% span to the shroud (100% span), the inlet 2 cases have reduced mainstream dissipation compared to their inlet 1 versions. Changing the inlet modifies the losses in the shroud boundary layer and within the span from the shroud to the 60% span location.

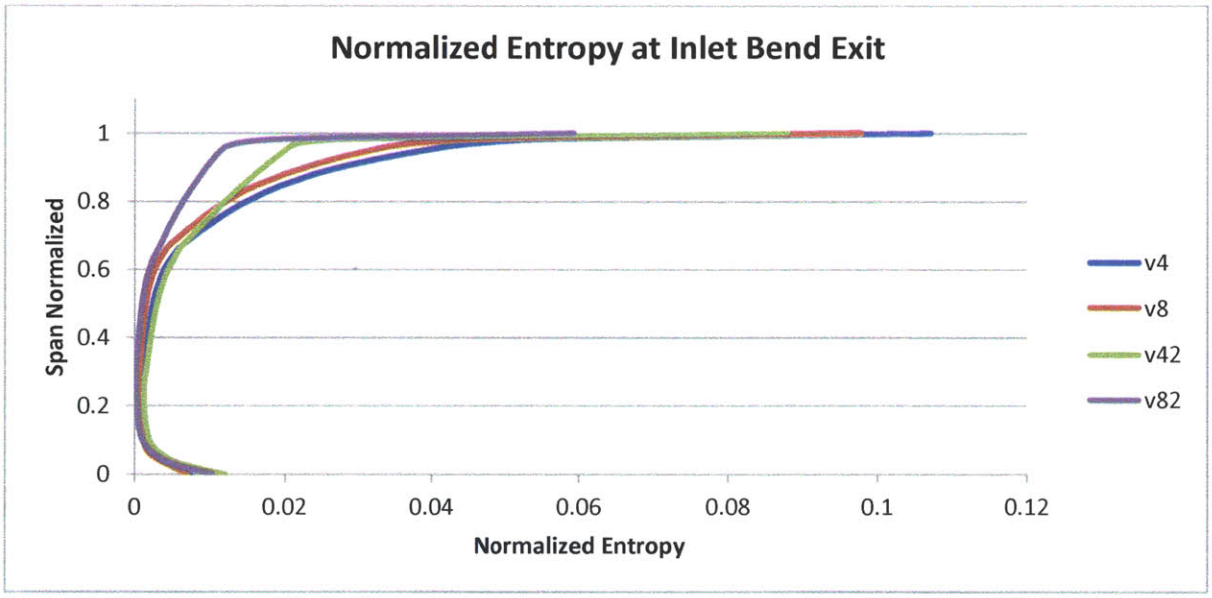

Figure 5-6: Normalized Entropy at Inlet Bend Exit for two cases with Inlet 1 (v4, v8) and two cases with inlet 2 (v42, v82)

5.3 Viscous Dissipation

The entropy of a fluid particle can be changed by heat addition and viscous dissipation. The rate of change of entropy per unit mass is [13]:

$$T\frac{Ds}{Dt} = \dot{Q} - \frac{1}{\rho}\frac{\partial q_i}{\partial x_i} + \frac{\Phi+\rho\epsilon}{\rho}$$

The heat source $\dot{Q}$ and heat flux q_i terms are negligible for these simulations. The viscous contributions to loss can be written as mean flow dissipation Φ and the turbulent kinetic energy dissipation ϵ. The viscous dissipation is several orders of magnitude higher than the turbulent kinetic energy dissipation in the bend and thus only the viscous dissipation will be considered for the rest of this analysis. The viscous dissipation in r-theta-z coordinates is [14]:

$$\Phi = 2\mu_E\left[\left(\frac{dV_r}{dr}\right)^2 + \left(\frac{dV_\theta}{d\theta}\frac{1}{r} + \frac{V_r}{r}\right)^2 + \left(\frac{dV_z}{dz}\right)^2 - \frac{1}{3}(\nabla\cdot V)^2\right] \quad (5.1)$$
$$+ \mu_E\left[\left(r\frac{d}{dr}\left(\frac{V_\theta}{r}\right) + \frac{1}{r}\frac{dV_r}{d\theta}\right)^2 + \left(\frac{1}{r}\frac{dV_z}{d\theta} + \frac{dV_\theta}{dz}\right)^2 + \left(\frac{dV_r}{dz} + \frac{dV_z}{dr}\right)^2\right]$$

where μ_E is the eddy viscosity. Equation 5.1 can be used to approximate the entropy generation in the bend. The change in entropy between two points along a streamline can be estimated roughly as:

$$\Delta s \sim \frac{\Phi}{\rho}\frac{\Delta l}{TU} \quad (5.2)$$

where Δl is a relevant length scale and U is a representative velocity. With the scaling model in Equation 5.2, the entropy rise in the inlet bend can be approximated based on measurable flow properties. The approximate entropy rise can then be compared with the CFD entropy rise output. This can help to determine if the viscous dissipation is an appreciable source of loss in the inlet.

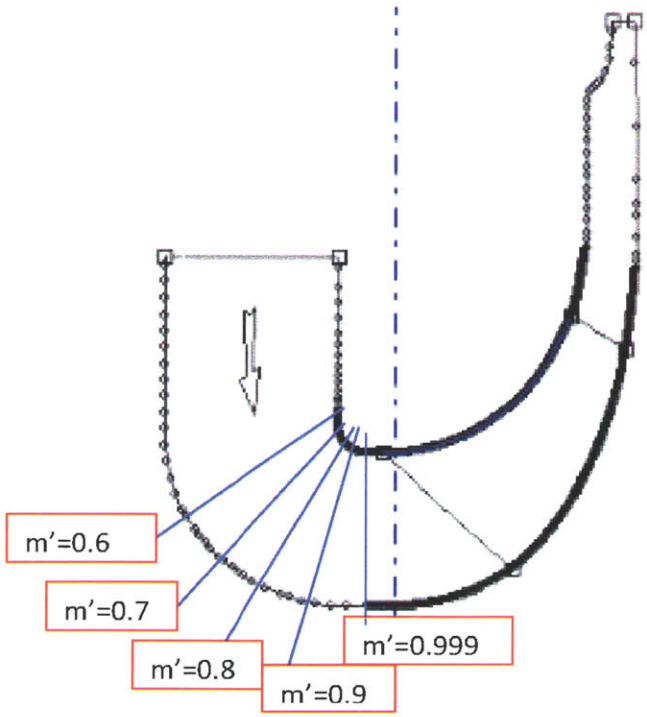

Figure 5-7: Passage Length locations for estimation of inlet dissipation

The inlet bend Δs, based on viscous dissipation, was calculated by tracing the flow properties in Equation 5.2 along streamlines and computing the quantity Δs between five planes within the inlet bend, as in Figure 5-7. The total Δs in the bend is the sum of these contributions. Using this approximation, the normalized entropy distribution is shown in Figure 5-8. The entropy calculated from the scaling model has similar trends to the actual entropy, with a minimum entropy rise near 20% span and an increase in entropy from 20% to the shroud. This implies that the viscous dissipation in the mainstream flow is not negligible.

This simple model underpredicts the normalized entropy in the region between 60% span and 90% span by a factor of 3-4, an effect of the scaling and the limited integration planes.

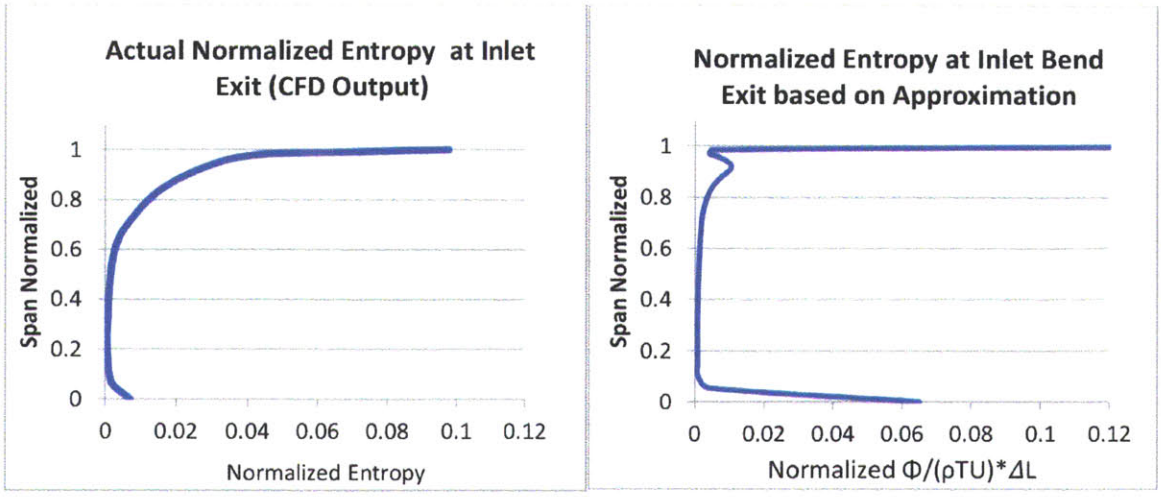

Figure 5-8: Comparison of Normalized Entropy for v8 based on CFD output and based on dissipation scaling

The terms $\mu_E \left(\frac{dV_r}{dz} + \frac{dV_z}{dr}\right)^2$ and $2\mu_E \left(\frac{dV_z}{dz}\right)^2$ are an order of magnitude or more higher than the other terms for v4 and v8. A spanwise-meridional, or n-m, form of these terms is commonly used in curved channel studies. The coordinate system is defined in Figure 5-9. The meridional coordinate is in the meridional direction and the spanwise coordinate is defined as 0 on the hub. Thus, the velocity components are defined as in Figure 5-10.

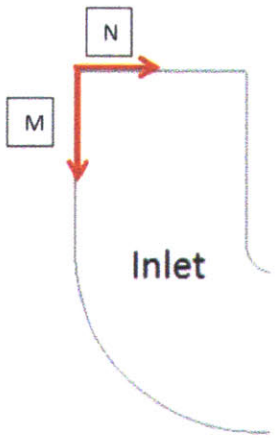

Figure 5-9: Coordinate System Definition

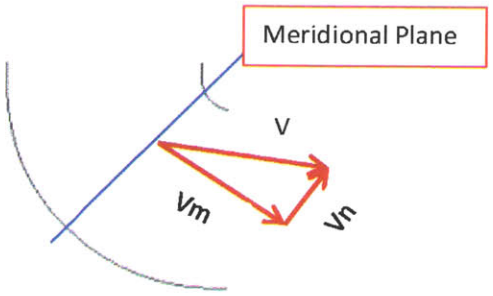

Figure 5-10: Spanwise and Meridional Velocity Definition

The main dissipation terms in the meridional and spanwise coordinate system are [15]:

$$\Phi_{Meridional,\,normal} = \Phi_N = 2 * \mu_t \left(\frac{dV_m}{dm}\right)^2 \qquad (5.3\ a)$$

$$\Phi_{Meridional\,\&\,Spanwise,\,shear} = \Phi_S = \mu_t \left(\frac{dV_m}{dn} + \frac{dV_n}{dm}\right)^2 \qquad (5.3\ b)$$

where "normal" represents the gradient of a velocity component in the direction of that component and "shear" represents the cross-term combining the gradients of velocity components with respect to another coordinate.

5.3.1 Mainstream Dissipation Correlations

The dissipation terms Φ_N and Φ_S in the previous section were examined at three meridional locations. The cases v4, v8, v42, and v82 were compared at 0°, 45°, and 90° (Inlet Bend Exit) as shown in Figure 5-11.

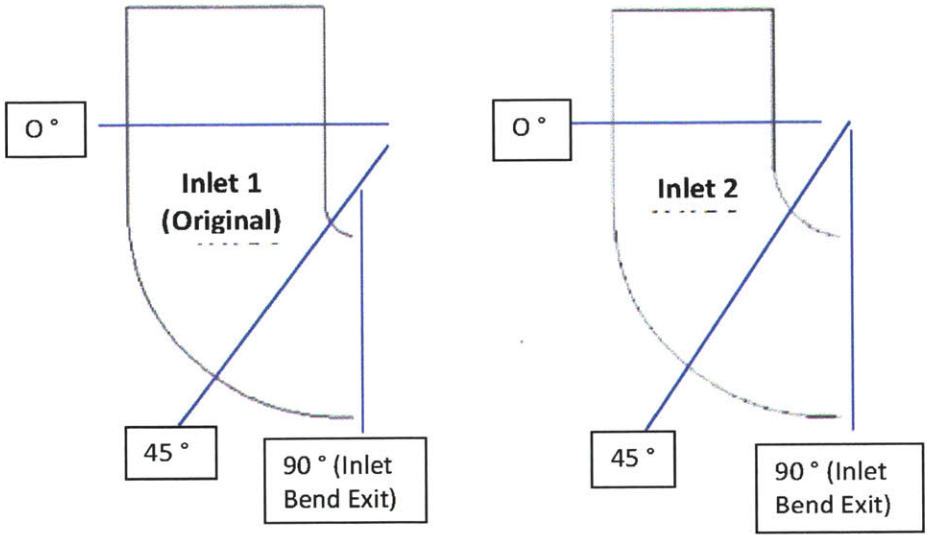

Figure 5-11: Measurement Planes for Inlet 1 and 2

Figure 5-12 and 5-13 show the quantities in Equations 5.3a and 5.3b at 45° and 90°, respectively, normalized by the square of the tip speed. Comparing v4 and v8, reducing the blade front loading reduces the meridional normal stresses at 45°, although both have higher values than with inlet 2 because of the more severe area contraction ratio. From the start of the inlet to 45°, the flow area reduces 50% with inlet 1 and 40% with inlet 2, and between 45° and 90°, the flow area reduces 20% with inlet 1 and by 17% with inlet 2.

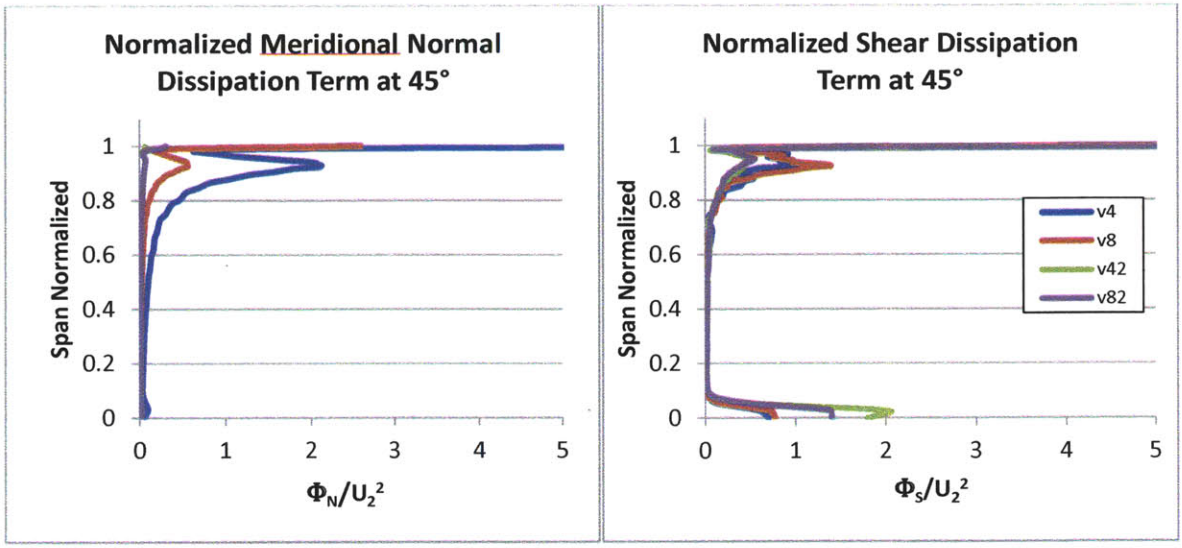

Figure 5-12: Dissipation Rates at 45°

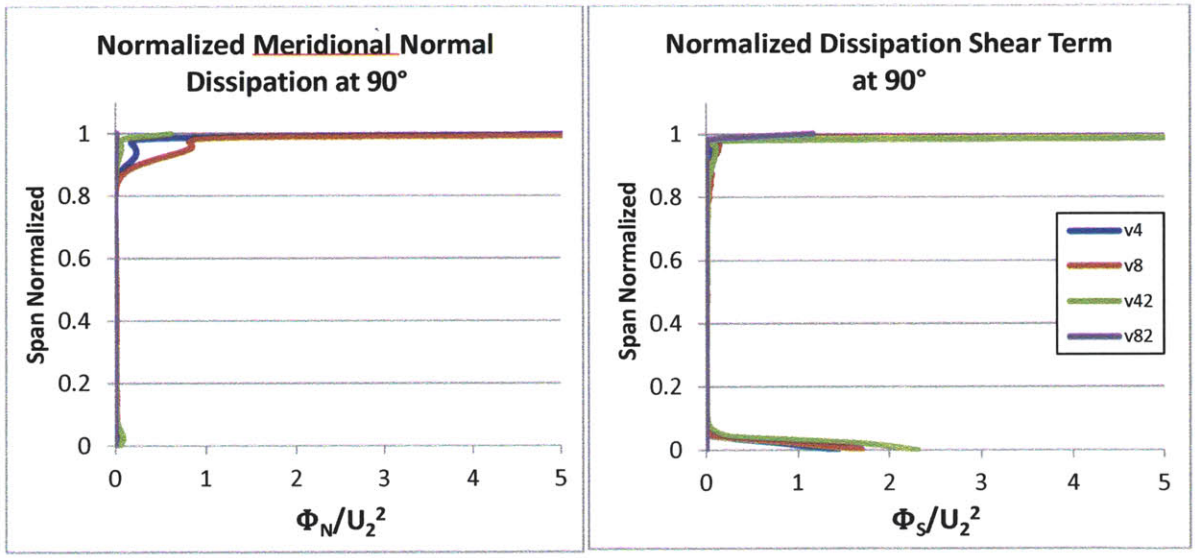

Figure 5-13: Dissipation Rates at 90°

Figure 5-13 shows that the computed dissipation rates outside the boundary layer at the 90° location are lower between 20% and 98% span than the rates at 45°, except for the meridional normal dissipation for v8. The lower blade front turning for v8, compared with v4, implies the former has a weaker upstream influence on the meridional normal dissipation as indicated in Figure 5-12. The change in mass flow-averaged meridional velocity between the 45° and 90° locations for v4 is 5% higher than that for v8. Figure

5-14 shows that low front turning on the shroud surface moves the throat downstream on the suction surface for v8. With high front turning as in v4, the throat is closer to the leading edge on the shroud surface, increasing meridional velocities at the inlet bend exit and increasing the meridional normal stresses for the inlet bend. The contribution to the mainstream dissipation by the shear term at 90° is negligible.

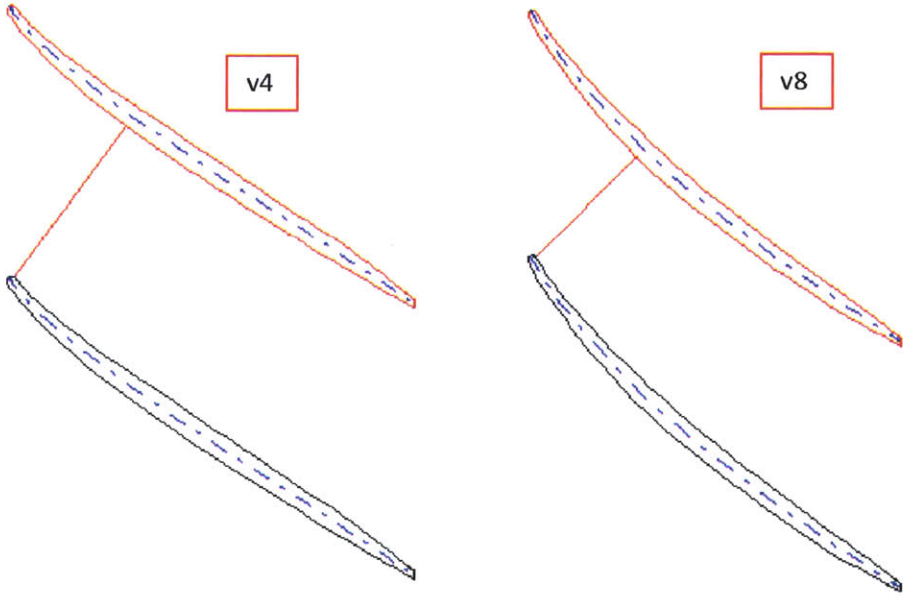

Figure 5-14: Throat Locations for v4 and v8 at Shroud

5.3.2 Boundary Condition Effects

The development of the velocity gradients in the inlet bend depends on the curvature of the bend and the downstream blade angle distribution. The velocity gradients also depend on the velocity profile of the flow entering the bend. Figure 5-15 shows the normalized meridional velocity $\frac{V_m}{U_{tip}}$ at the inflow boundary condition. Meridional velocity near the shroud is as much as 7% larger than the meridional velocity near the hub, outside the boundary layer. The inflow boundary condition sets the mass flow, stagnation pressure, and stagnation temperature. In the bend, the meridional velocity on the shroud increases, as in Figure 5-16.

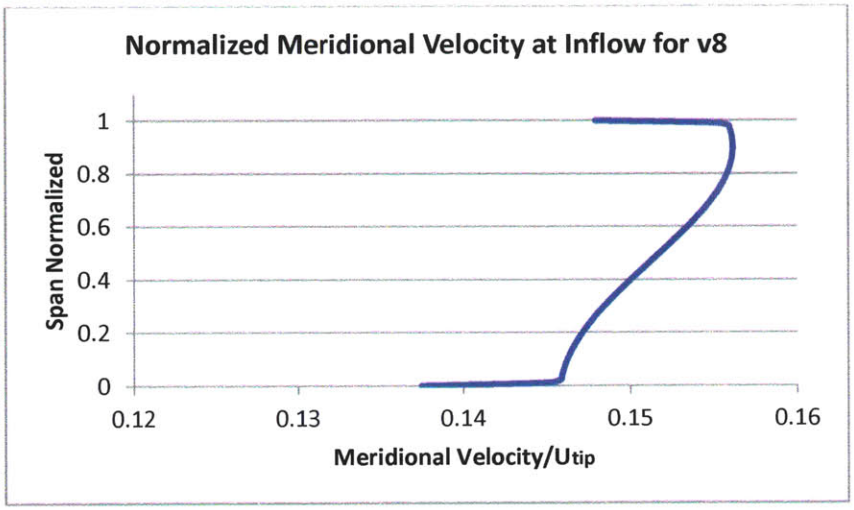

Figure 5-15: Normalized Meridional Velocity at Inflow (Boundary Condition)

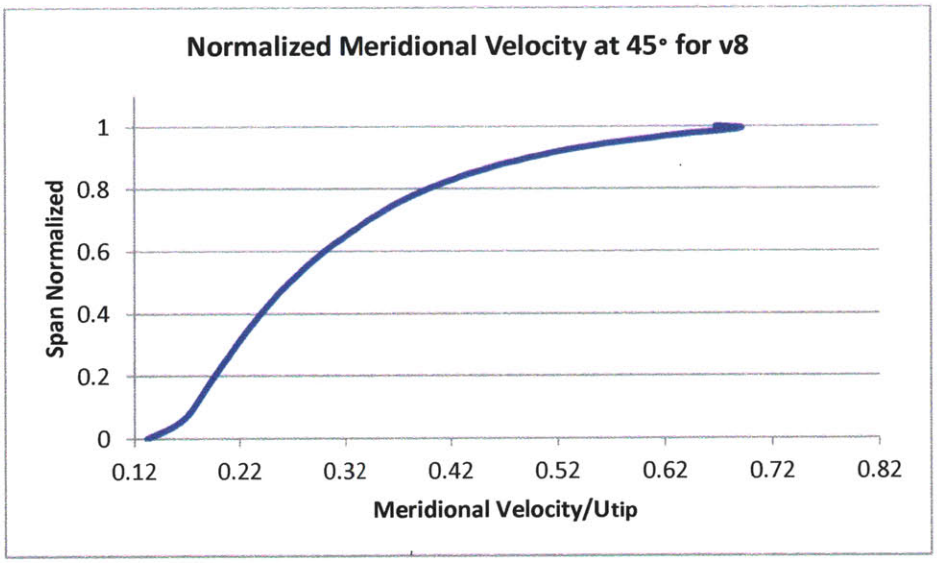

Figure 5-16: Normalized Meridional Velocity at 45° for v8

Chapter 6

Quasi-3D Blade Boundary Layer Analysis with MISES

6.1 Motivation

The leading edge region up to the 20% passage length was identified as a region of interest in Chapter 4. The connection between reduced front turning near the casing and lower losses can be seen in the 3D analysis, but it is not yet clear how the geometry affects the blade boundary layers. A quasi-3D analysis was thus performed using MISES to determine the boundary layer behavior and to help link the losses to the blade geometry.

6.1.1 Case Study Parameters

MISES requires a boundary condition specification, a streamtube height definition, and a turbulence intensity. Increased turbulence intensity moves the transition point closer to the separation point, although experiments show that beyond 3% turbulence intensity, increasing the intensity level does not affect transition [21]. We examined the blading for three cases: v4, v5c, and v8 at 20%, 55%, and 90% span. The inlet relative Mach number and relative flow angle, extracted from CFD, was specified a blade chord upstream of the LE. The CFD flow was divided into 14 streamtubes of equal mass flow, and 4 streamtubes were chosen for each span to enclose the full 20%, 55%, or 90% span blade geometry.

6.1.2 Input Geometries of Select Cases

Figure 6-1 shows the blade geometries at each span. They are plotted against a streamwise location, M', which is 0 at the LE and computed along the blade up to the TE in reference to neighboring points on the blade[1]:

$$M_i' = M_{i-1}' + \frac{2}{r_i + r_{i-1}}\sqrt{(r_i - r_{i-1})^2 + (z_i - z_{i-1})^2}$$

where r and z represent the radial and axial location of the points defining blade. The θ coordinate describes the location of a point on the blade surface in the theta direction.

The impellers differ in loading near the hub and shroud. At the 90% span location, v8 has the smallest blade angle change in the front region of the blade (M'<0.2), and v4 has the largest. At the 55% span location, the three impellers have similar turning. At the 20% span location, v8 has the largest turning in the front region of the blade.

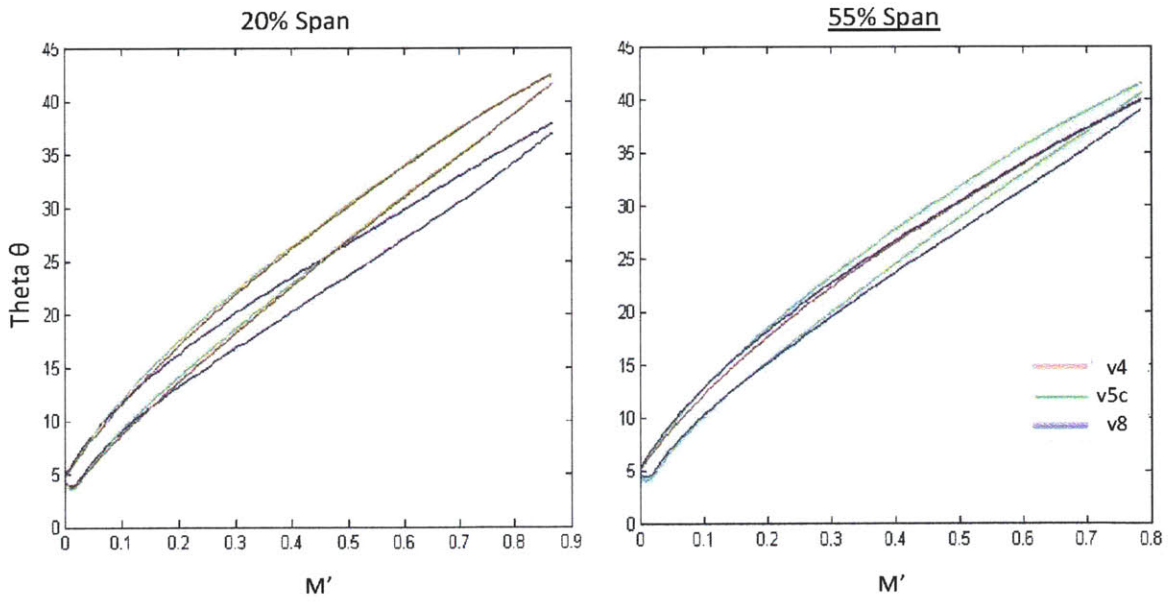

[1] MISES documentation, 2.6.7

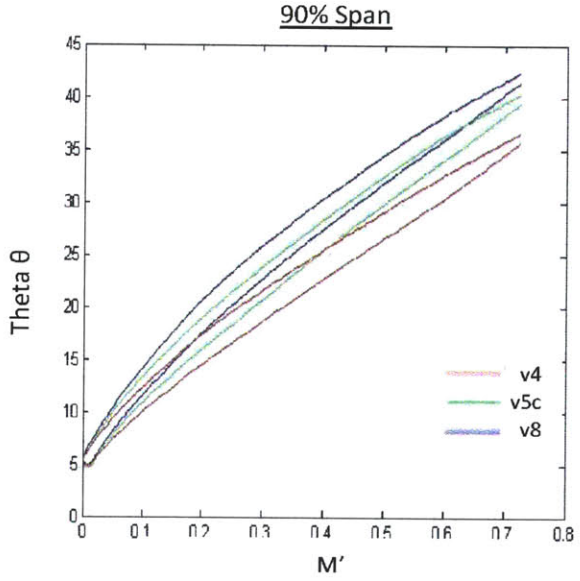

Figure 6-1: Blade Geometries at three span locations for MISES Input

To calculate the streamtube height, points dividing the circumferentially mass-averaged streamtubes of equal mass flow were tracked at 20 spanwise locations along the flowpath. Figure 6-2 shows the streamtube heights for the cases examined, normalized by the streamtube height at the leading edge. At 90% span near the leading edge there is an increase in streamtube height for v8 and for v5c, and a decrease for v4. The converse is true at 20% span, where v4 has an increase in streamtube height near the LE, and the streamtube height for v8 decreases most rapidly.

The normalized meridional velocity $\frac{V_m}{U_{tip}}$ distribution is shown in Figure 6-3. With low front turning at the shroud and high front turning at the hub, v8 does not have as much acceleration on the shroud as on the hub and has higher meridional velocities on the hub than the other cases.

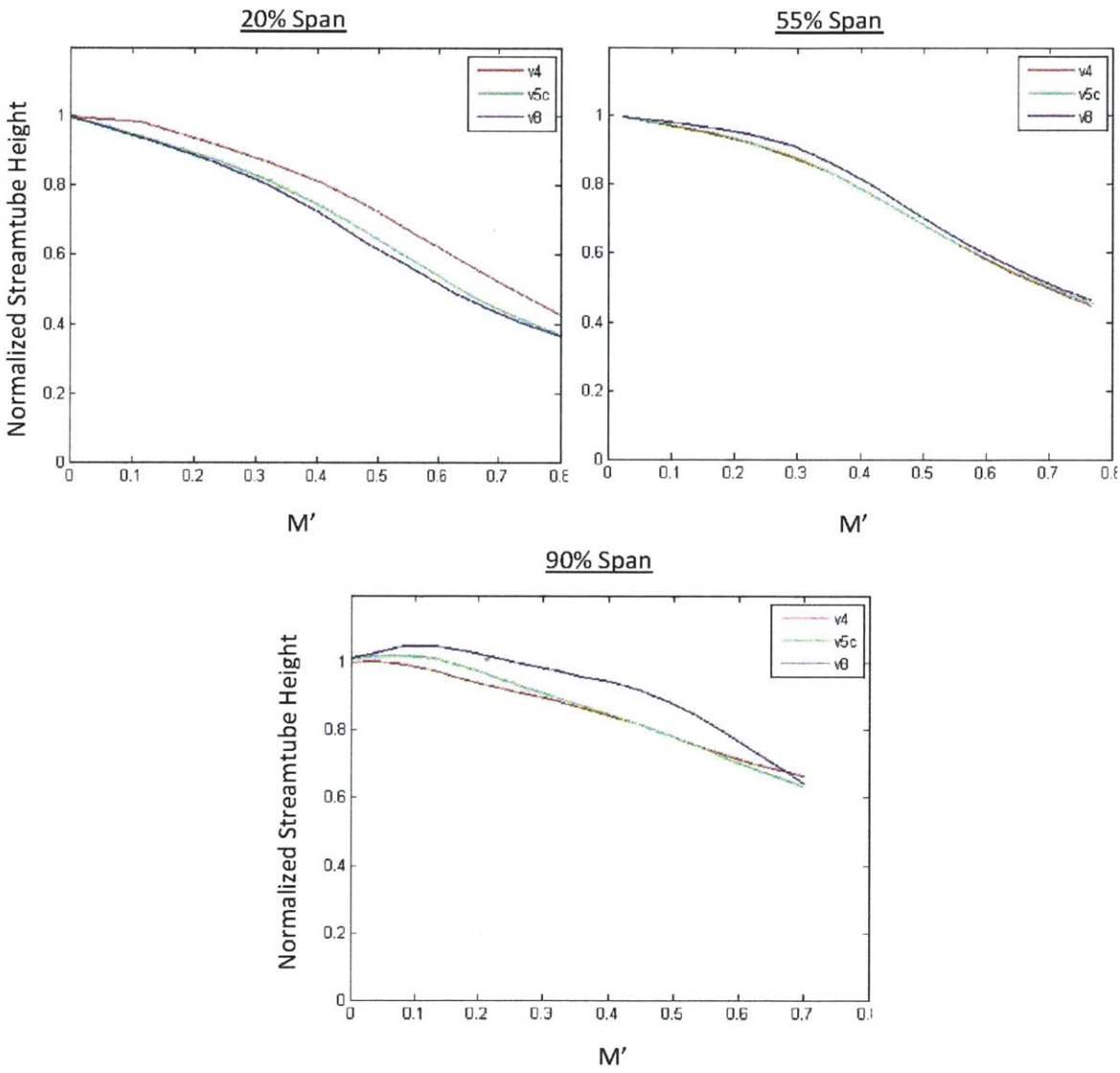

Figure 6-2: Normalized Streamtube Height for Select Cases

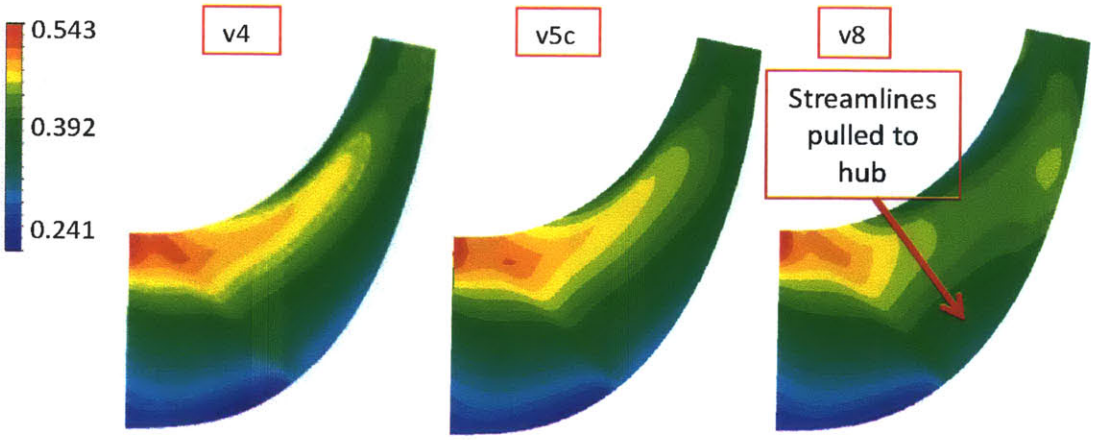

Figure 6-3: Normalized Meridional Velocity V_m/U_{tip}

The largest decrease in meridional velocity on the shroud occurs for v8, but this is not necessarily the case for the overall deceleration. The relative Mach number contours at 90% span in Figure 6-4 indicate that the deceleration near the shroud for v8 is the smallest of the three cases. v4 has the highest peak relative Mach number at 90% span, due to the positive incidence, with a stagnation point on the pressure side and acceleration around the leading edge, giving high velocities, as in Figure 6-5.

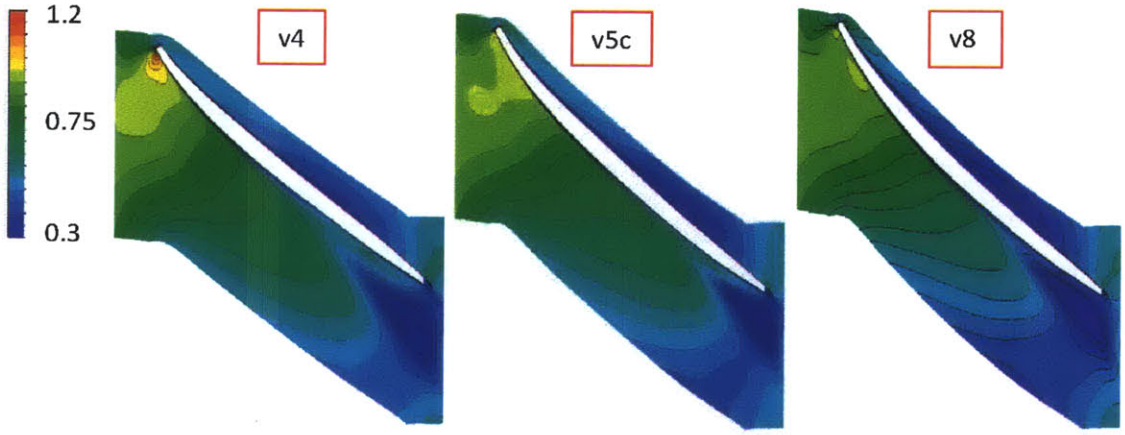

Figure 6-4: Relative Mach number at 90% Span

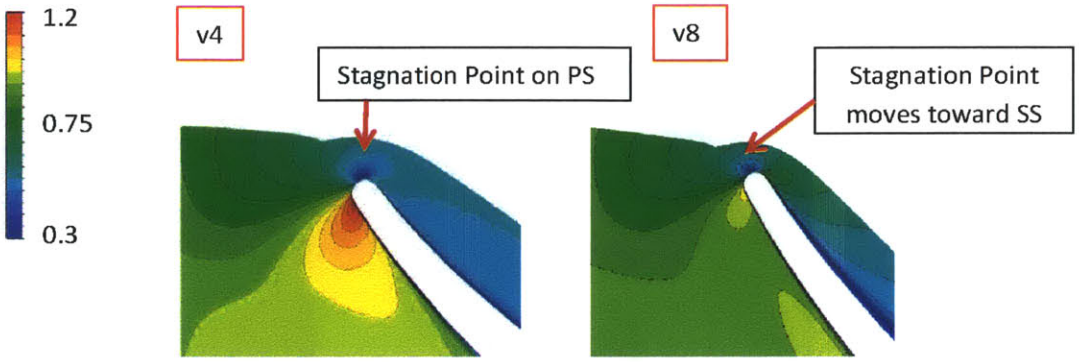

Figure 6-5: Relative Mach number for v4 and v8 near LE showing stagnation point moving from PS (Pressure Side) to SS (Suction Side) for reduced incidence

6.2 Boundary Layer Examination

6.2.1 CFD vs. MISES

We wish to assess the MISES results and connect them with the three-dimensional CFD. Figures 6-6, 6-7, and 6-8 show MISES and CFD blade loading distributions for 20%, 55%, and 90% span geometries, respectively. The blade loading distribution is based on C_p, defined in Section 3.1. Each figure highlights the region of interest, as given from the CFD calculations. The 20% passage length region in CFD showed a trend of overall losses with front region deceleration (Chapter 4). The front region corresponds to about 10% blade chord for all cases[2]. In this region, the values of the MISES Cp are within 3% of the CFD values, with the exception of the 90% span v4 case with differences of ~10%. Downstream of 10% chord location, the MISES and CFD loading distributions do not match because of secondary flow on the latter part of the blade, and the quantitative utility of the MISES results in the latter part of the blade is thus limited.

At 55% and 90% span, v5c and v8 have a plateau on the suction surface in the region of interest, such that the peak relative Mach number is further downstream than that for v4. In the region of interest, v4 has an adverse pressure gradient from hub to shroud, whereas v5c and v8 have favorable pressure gradients in the region of interest at 55%

[2] Note: 0% "Passage length" is at the inlet bend exit, not at the LE. The inlet bend exit corresponds to the start of the shrouded, rotating domain. Thus, percent blade chord does not equal percent passage length. The passage length is a unit normalized by the length of the full rotating domain.

and 90% span with a more favorable pressure gradient at 90% span than at 55% span for both v5c and v8.

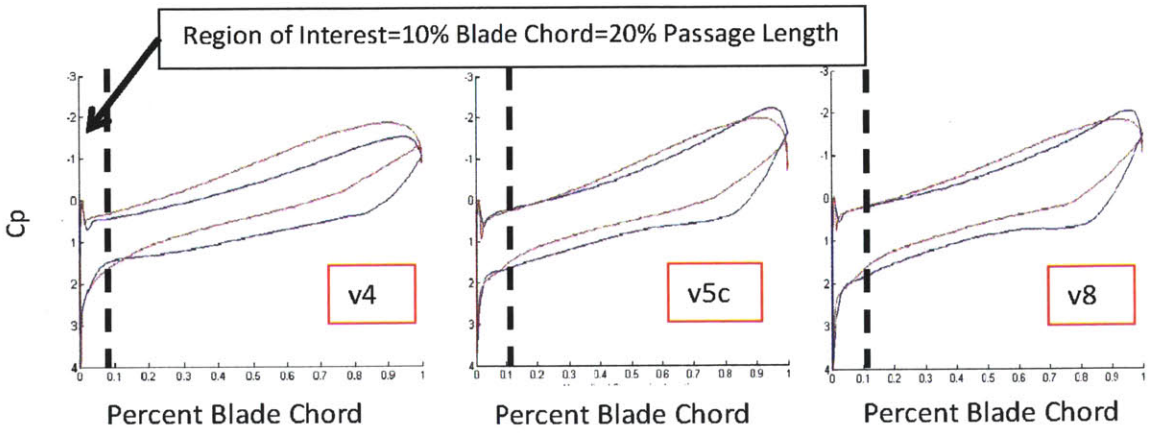

Figure 6-6: CFD(Red) vs. MISES(Blue) Blade Loading Distributions at 20% Span

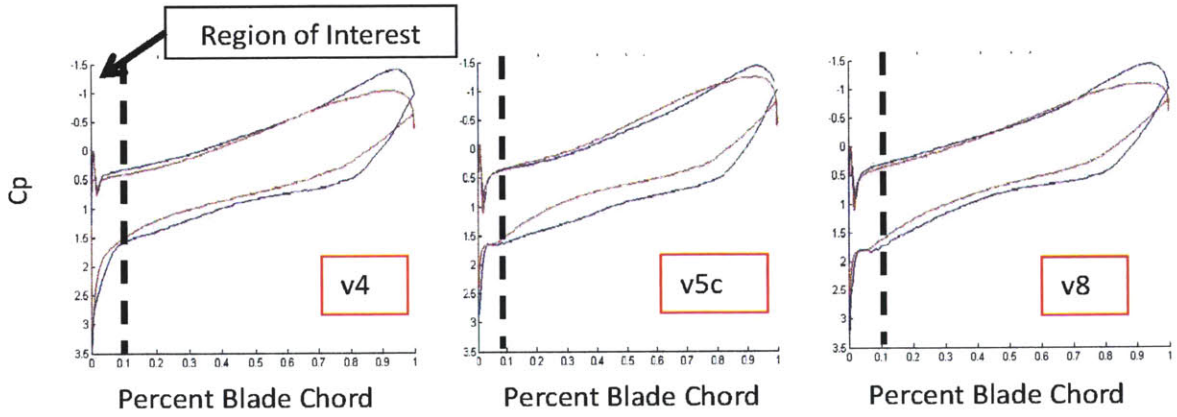

Figure 6-7: CFD(Red) vs. MISES(Blue) Blade Loading Distributions at 55% Span

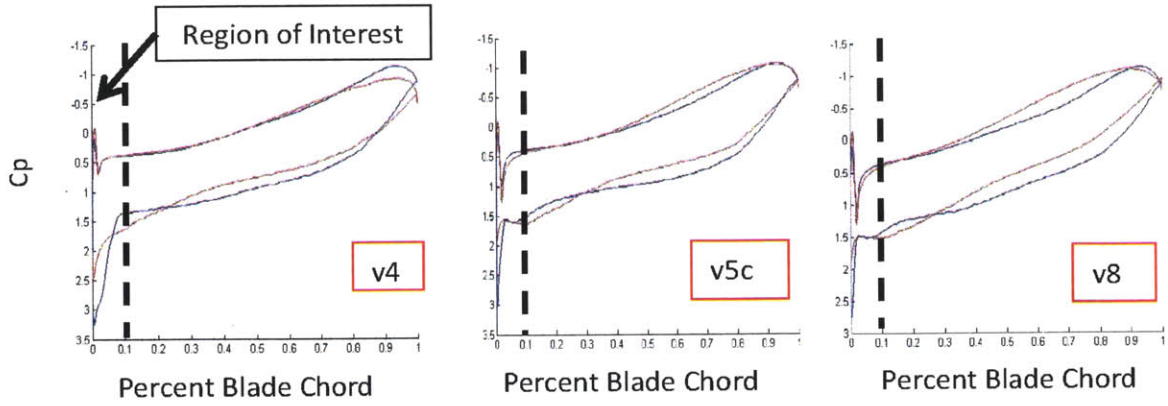

Figure 6-8: CFD(Red) vs. MISES(Blue) Blade Loading Distributions at 90% Span

6.2.2 Boundary Layer Analysis

We can compare the different cases using the shape factor $H = \frac{\delta^*}{\theta}$ and the momentum thickness θ for each span geometry. The parameters are related by the Von Karman equation:

$$\frac{d\theta}{dx} + (H + 2 - M_E^2)\frac{\theta}{U_E}\frac{dU_E}{dx} = \frac{C_f}{2}$$

which describes the state of the boundary layer in a 2D flow. The shape factor rises with adverse pressure gradient [3] and indicates transition by dropping to a value of 1.4[3]. It can also indicate a separation bubble by rising to roughly 3[4]. The momentum thickness is related to the viscous loss, which MISES defines its viscous loss parameter as [23]:

$$\omega_v = \frac{1}{P_{t1} - P_1}\left(\frac{P_t}{P}\frac{\rho V}{\dot{m}}\rho_e V_e^2 \theta b\right)_{exit}$$

The viscous loss is proportional to $(\rho_e V_e^2 \theta)_{exit}$, which is the defect in streamwise momentum flux between the actual flow and a uniform flow with properties ρ_e and V_e [18]. The quantity b is the streamtube height normalized by the inlet streamtube height. The trailing edge momentum thicknesses on the pressure side for all spans and cases were 3-4 times smaller than the suction side momentum thicknesses at the trailing edge,

[3] Personal communication with Dr. M. Drela, MIT, March 2014.
[4] See previous footnote.

indicating that the suction side is responsible for most of the boundary layer loss. Only suction side surface boundary layer parameters are shown in the following figures.

The goal is to assess the links between the boundary layer behavior and the deceleration and loss trends seen in the front 20% passage length in Chapter 4. Table 6-1 shows the viscous loss computed by MISES. At 20% span, the loss values are not distinct. For 55% span, v4 has the largest loss, due to incidence on the blade. At this span, v5c performs better than v8 in this region with 3% lower losses, although the 3D calculations show that v8 has lower loss generation in the front region of the blade. Thus, the smallest boundary layer loss at this span does not correlate with the smallest losses calculated with the 3D CFD.

	20% Span	55% Span	90% Span
v4	0.050	0.044	0.048
v5c	0.050	0.032	0.026
v8	0.050	0.033	0.023

Table 6-1: MISES Loss Coefficients

In Figure 6-9, at 90% span, both v5c and v8 have a laminar separation bubble near the leading edge. The v4 blade transitions without separation as indicated by the drop in shape factor at M'=0.03. While transitioning to turbulent flow, the flow separates from the suction side, generating the turbulent separation bubble seen near M'= 0.05, causing the momentum thickness to increase. The overall losses calculated by MISES are thus increased.

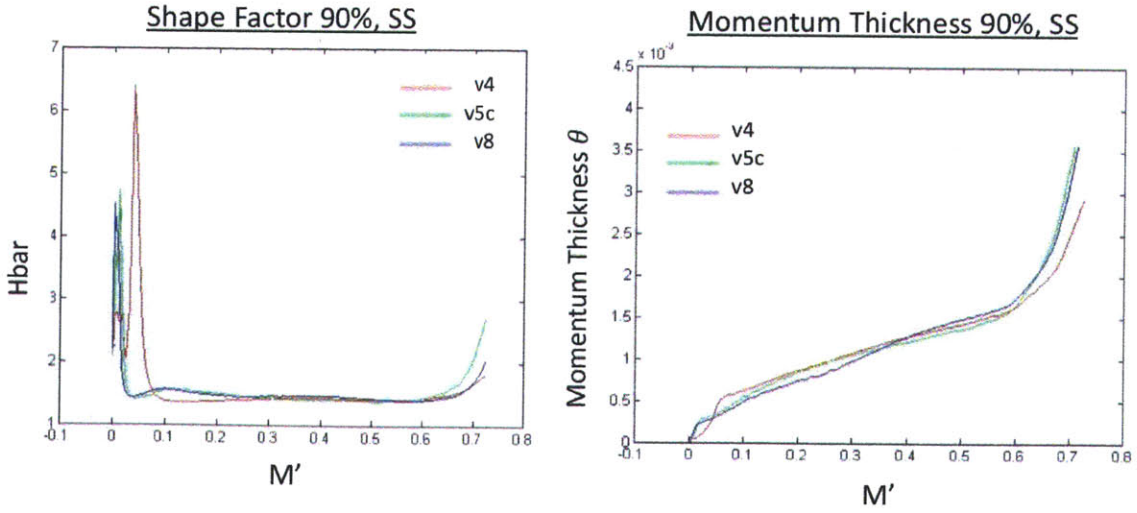

Figure 6-9: Boundary Layer Parameters for 90% Span

6.2.3 Linking Boundary Layer Analysis to 3D Loss Trends

The two-equation models in the 3D computations assume the boundary layer is turbulent starting at the leading edge [24]. Separations are thus turbulent separations. MISES, however, uses modified Abu-Ghannam Shaw experimental correlations to estimate natural, bypass, and separation-induced transition [24] as well as laminar and turbulent regimes. The "fully turbulent" assumption is used in many turbomachinery applications due to the transition near the leading edge [22] with high Reynolds number and turbulence intensities >3%. This situation is seen in Figure 6-9, where a 5% turbulence intensity level in MISES gives separation-induced transition within <1% chord. The laminar separation bubble can affect the value of the loss coefficient calculated by MISES, and the behavior of the turbulent boundary layer with respect to the pressure gradients is captured.

As MISES is most appropriate where there are not regions of significant crossflow, we compare the momentum thickness at the 10% blade chord location. At 90% span, the momentum thickness for v5c and v4 are, respectively, 11% greater and 24% greater than that for v8., MISES thus captures the trend in overall loss increase in this region (shown in Figure 4-9), where v8 has the least loss increase and v4 has the highest loss increase.

For a nearly constant skin friction, which occurs after the transition point for all cases, the Von Karman equation implies change in momentum thickness is proportional to the value of the momentum thickness after transition and the pressure gradient. While the value of the momentum thickness after transition is not captured in the CFD, the change in momentum thickness due to pressure gradients is captured. The relative Mach number distributions in Figure 6-10 indicate that the peak relative Mach number on the suction side is moved downstream for v5c and v8, compared to v4 whose peak Mach number is near the leading edge. Impeller v8 shows an acceleration region from the leading edge to ~9% chord, while v5c has an acceleration region from the leading edge to ~6% chord. The low front turning for v8 thus moves the peak relative Mach number downstream so $\frac{dU_E}{dx}$ for v8 is larger than for v5c, which implies $\frac{d\theta}{dx}$ for v8 is less for v5c. The local negative

pressure gradients in the front region of the blade (<10% chord), generated from the low front turning near the shroud, reduce the growth of the momentum thickness.

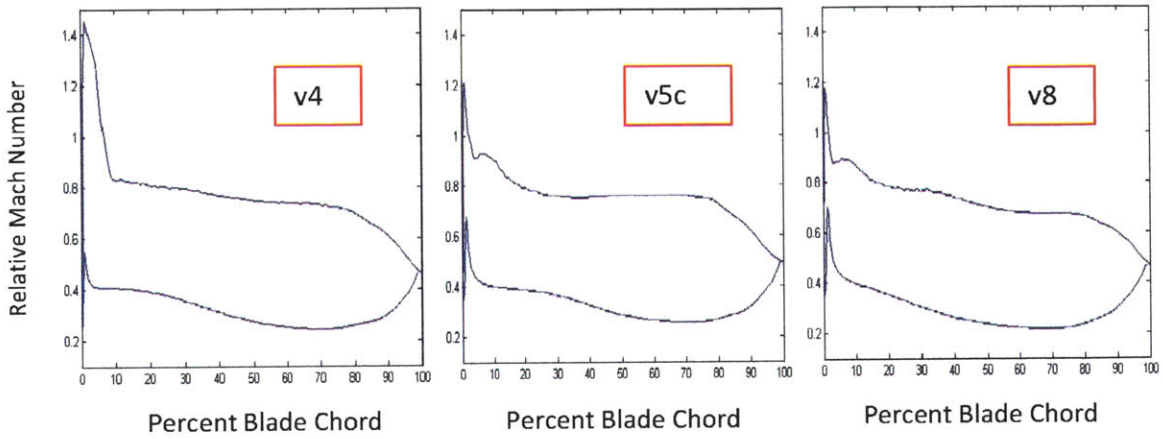

Figure 6-10: Relative Mach number Distribution at 90% Span

6.3 Chapter Summary

In this chapter, the boundary layer development in the front region of the blade was examined using a quasi-3D MISES code. Three span locations were examined. The values of C_p front 10% blade chord in MISES were within 3-10% of the 3D CFD C_p values. The momentum thickness at the 90% span, 10% blade chord location correlated with the loss increase in the front region of the blade seen in Figure 4-9. High turbulence intensity promoted transition within the first <1% blade chord, and the trends in the MISES boundary layer development can be compared with the fully turbulent CFD boundary layer. Lower front turning moved the peak relative Mach number downstream, reducing the change in momentum thickness in the front region of the blade.

Chapter 7

Secondary Flow and Losses

7.1 Motivation

In this chapter, we describe the losses in the region from 20% passage length to the impeller exit. With the original inlet, v5c had 12% lower losses than v4, and v8 had 6% lower losses than v4 in the post-20% passage length region. With inlet 2, v5c2 has 15% lower losses in this region than v42, and v82 has 18% lower losses than v42 in the post-20% passage length region. Between the inlet exit and 20% passage length, v8 has the lowest losses. However, the losses for v8 in the post-20% passage length region are larger than those for v5c with inlet 1. This chapter will investigate the cause of the losses in this region.

7.2 Secondary Flow Losses and Mitigation

7.2.1 Secondary Flow Effects

The normalized entropy plots in Chapter 4 show the migration of a high entropy region toward the suction side corner for all impellers. The normalized entropy contours on the leading edge and trailing edge planes are shown in Figure 7-1. Figure 7-1 (b) and (c) show the movement of the loss region from the blade boundary layer near the leading edge to the shroud surface at the trailing edge, indicating the presence of secondary flow.

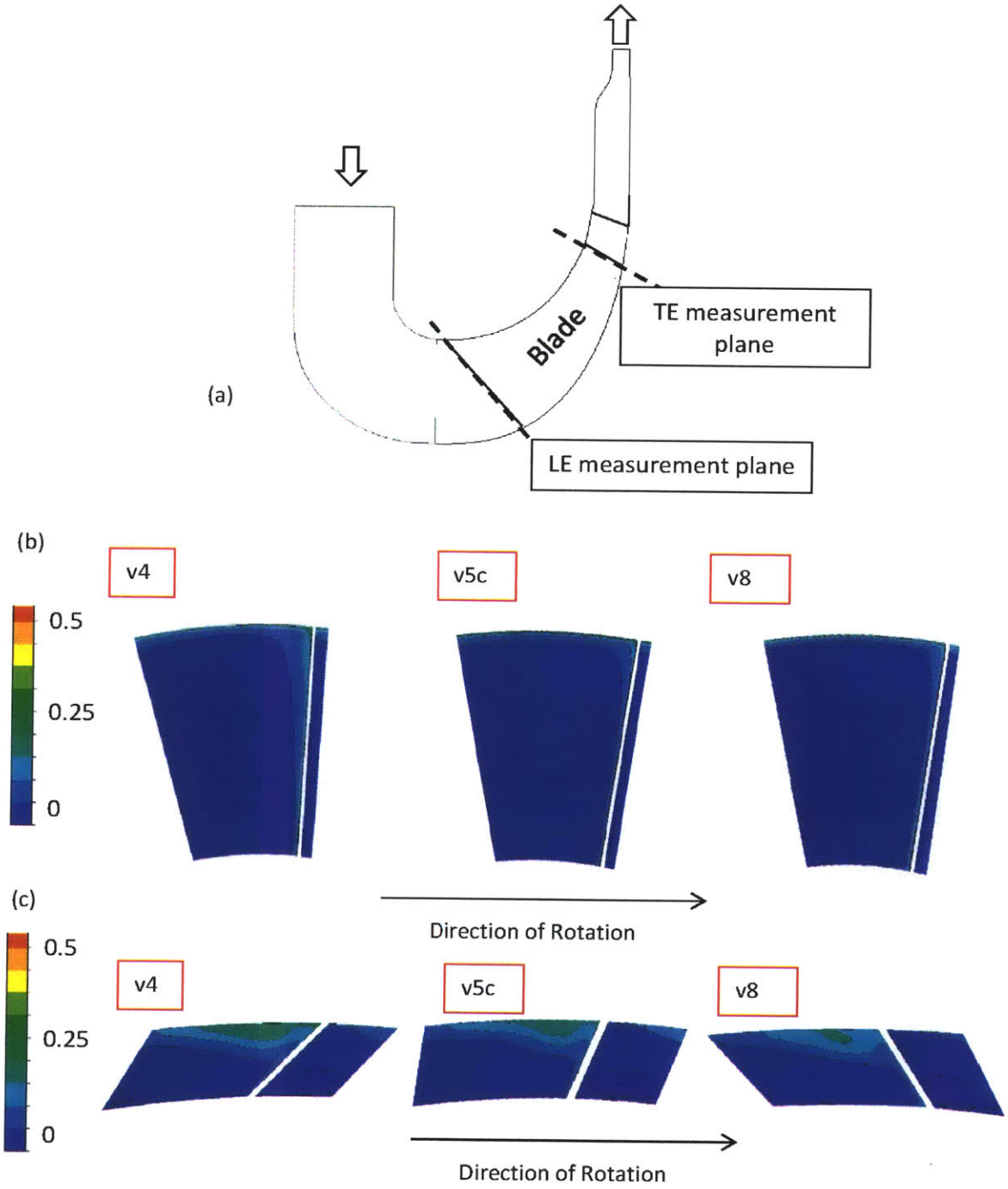

Figure 7-1: Location of the Leading Edge and Trailing Edge measurement planes in (a) and the normalized entropy in those planes, respectively in (b) and (c)

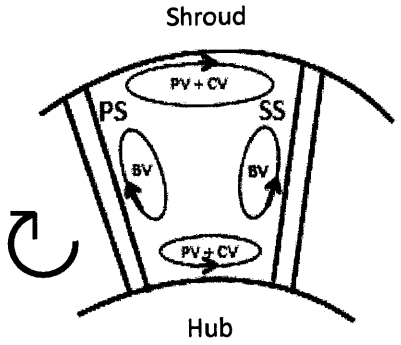

Figure 7-2: Secondary flow induced by Passage Vortices (PV), Coriolis Vortices(CV), and Blade Surface Vortices(BV) [25]

The loss region at the trailing edge, referred to as the wake, is at different locations for each case in Figure 7-1 (c) because the intensity of secondary flow in the impeller determines the location of the wake at the exit. The direction of the secondary flow is determined by the ratio of passage vortices (PV), blade surface vortices (BV), and Coriolis vortices (CV). These are shown schematically in Figure 7-2. They are defined by [25]:

$$d\left[\frac{\Omega_s}{W}\right]_{PV} \approx \frac{2}{\delta_{h,s}}\left(\frac{ds}{R_t}\right)$$

$$d\left[\frac{\Omega_s}{W}\right]_{CV} \approx \frac{\omega}{\delta_{h,s}}\left(\frac{ds}{W}\right)$$

$$d\left[\frac{\Omega_s}{W}\right]_{BV} \approx \frac{2}{\delta_{PS,SS}}\left(\frac{ds}{R_m}\right)$$

where $d\left[\frac{\Omega_s}{W}\right]$ represents the rate of change of streamwise vorticity over relative velocity [25], ω is the rotational speed, R_t is the radius of curvature of a streamline in the radial-theta plane, and R_m is the radius of curvature of a streamline in the radial-axial plane. The ratios of the sum of the first two quantities over the third quantity determine the position of the wake.

A way to visualize the effect of the ratio of these vortices, described above, is to examine the gradients of reduced pressure [6], which we derived as:

$$P_r = P * \frac{\left(\frac{T_t^*}{T}\right)^{\frac{\gamma}{\gamma-1}}}{(P_{trel}/P)}$$

In the above expression, P_{trel} is the relative stagnation pressure[5] and T_t^* is the rotating stagnation temperature defined as:

$$T_t^* = T_{trel} - \frac{W^2}{2C_p}$$

In rotating machinery, the change in rotary stagnation pressure correlates with the increase in entropy and was derived as:

$$P_t^* = P\left(\frac{T_t^*}{T}\right)^{\frac{\gamma}{\gamma-1}}$$

The maximum value of P_t^* is upstream of the impeller, and low momentum fluid moves to regions of low P_r. A normalized form of the reduced pressure defined in [6, 27] can be used to track the secondary flow intensity in the impeller:

$$P_r' = \frac{P_{t\,upstream}^* - P_r}{P_{t\,upstream}^* - P_{t\,TE}^*}$$

Higher values of P_r' indicate lower values of P_r. Controlling differences of reduced static pressure can reduce the secondary flows and hence the overall impeller and stage losses [6].

Figure 7-3 shows the normalized reduced pressure blade loading diagrams on the hub (blue) and the shroud (red). At both hub and shroud, there is lower reduced pressure on the suction side, thus higher P_r'. ΔC_p represents the difference in reduced pressure between the suction and pressure sides, which drives the secondary flow between those surfaces. $\Delta C_{p,B}$ represents the difference in reduced pressure between the hub and shroud.

[5] P_{trel}/P is the same as P_t^*/P_r. Either can be used, but the former was chosen for simplicity.

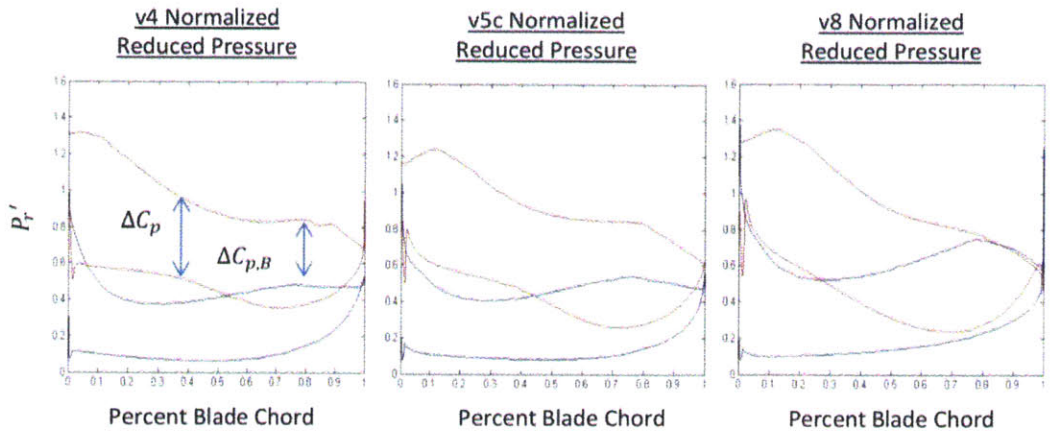

Figure 7-3: Normalized Reduced Pressure on Shroud(Red) and Hub(Blue)

The secondary flow has less effect in the front region of the blade due to the thin boundary layers. Figure 7-3 shows that as the flow approaches the trailing edge, $\Delta C_{p,B}$ decreases. $\Delta C_{p,B}$ is least for v8, so the secondary flow from hub to shroud on the blade surface is the least for v8. This explains the larger loss regions on the suction surface near the hub for v8 compared to the other cases, as in Figure 7-1(c); reduced secondary flow from hub to shroud reduces loss. The boundary layer on the suction surface is thickest for v8 and the high entropy region is closer to the suction surface for v8, indicating that the secondary flow carrying low momentum fluid up the suction surface is weaker than for v4 or v5c.

The losses due to hub to shroud secondary flow are least for v8, but the overall losses for v8 are 6% higher than v5c in the post-20% passage length region. This can be explained by the ΔC_p on the pressure side. In Figure 7-3, ΔC_p on the pressure side near the trailing edge is highest for v8 compared to the other two cases. This causes the buildup of low momentum fluid on the suction side hub corner, which can be seen in Figure 7-1. The buildup of low momentum fluid in the suction side hub corner leads to the increase in losses for v8 in the post-20% region. It will be shown in the next section that this is an effect of the blade lean.

7.2.2 Blade Lean Effects

Figure 7-1 (c) shows the different impeller blade leans. These are a consequence of keeping the throat the same for different casing blade angle distributions. The impellers have linear element blades (See [7]), with the hub and shroud blade angles defined in BladeGen, and the 3D blade defined by linearly connecting the hub and shroud blade angles. Blade lean is defined by the *lean angle* γ between the suction surface and shroud wall [7], as in Figure 7-4. Negative lean, i.e. the blade at the hub leading the blade at the shroud in the direction of impeller rotation, has been found to suppress secondary flows in centrifugal compressors [6], but it also promotes the buildup of low momentum fluid in the suction side hub corner, which can increase loss [7].

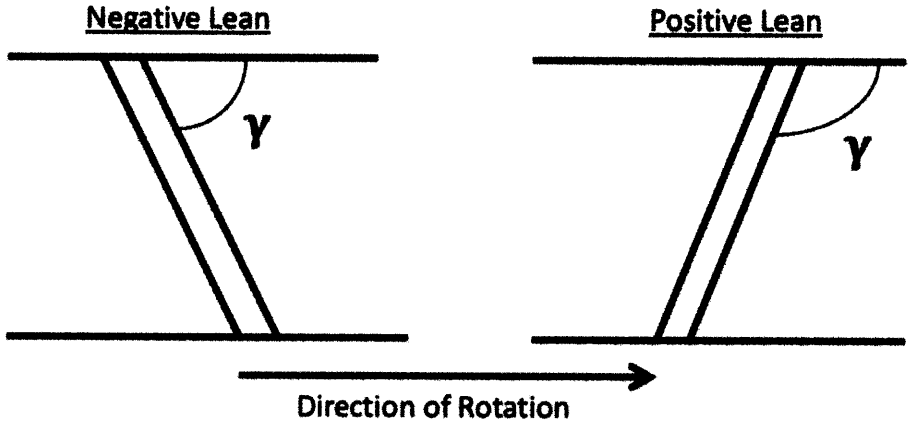

Figure 7-4: Definitions of Positive and Negative Lean

Impeller v4 has positive lean with γ=135°, v5c has reduced positive lean with γ=115°, and v8 has negative lean with γ=55°. Negative lean decreases the secondary flow from hub to shroud, which is correlated with less overall loss. With reduced secondary flow from hub to shroud, it has been found that there is an increase in secondary flow from pressure side to suction side [7]. This situation is seen in Figure 7-3 where $\Delta C_p \gg \Delta C_{p,B}$ for v8. The increased reduced pressure differences between the suction and pressure surfaces explains the low momentum flow buildup for v8 near the hub, which can be seen in the contours of meridional velocity normalized by blade tip speed in Figure 7-5. The negative blade lean in v8 carries low momentum fluid to the suction surface, where it interacts with the blade surface boundary layer, increasing the losses in the post-20%

region for v8. Thus, while v8 has the least losses in the suction side shroud corner, the pressure side to suction side secondary flow on the hub increases the losses.

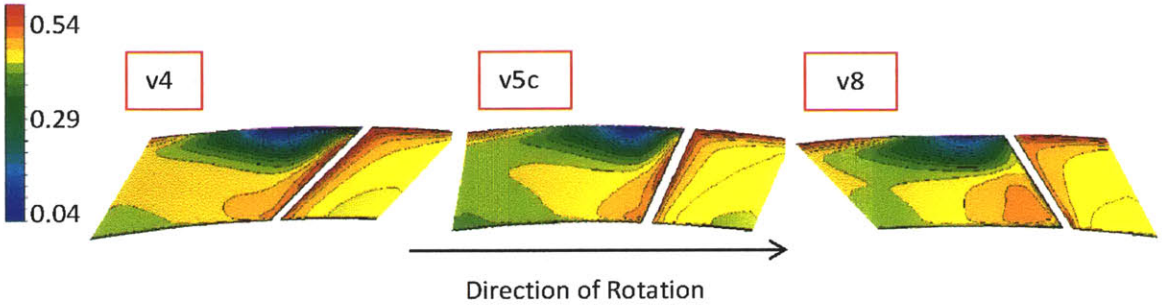

Figure 7-5: Normalized Meridional Velocity $\frac{V_m}{U_2}$ in Wake Region at Trailing Edge

7.2.3 Secondary Flow Loss with Inlet 2

Normalized entropy distributions at the trailing edge for the cases with inlet 2 are shown in Figure 7-6. At the TE, the high entropy region is reduced for these cases compared to their inlet 1 versions. Losses generated in the post-20% passage length region for v42 and v5c2 show small changes from the original inlet versions (less than 1%). Lower losses at the TE for v42 and v5c2 are due to reduced losses upstream of 20% passage length. There is a loss decrease of 12% from v8 to v82 in the post-20% passage length region. Figure 7-7 shows the buildup of low normalized meridional velocity (low momentum fluid) near the suction side hub corner for v82, as with inlet 1, leading to an increase in entropy in the suction side hub corner (See Figure 7-6). There is an increased meridional velocity uniformity across the span, indicating a reduction of secondary flow [6, 7].

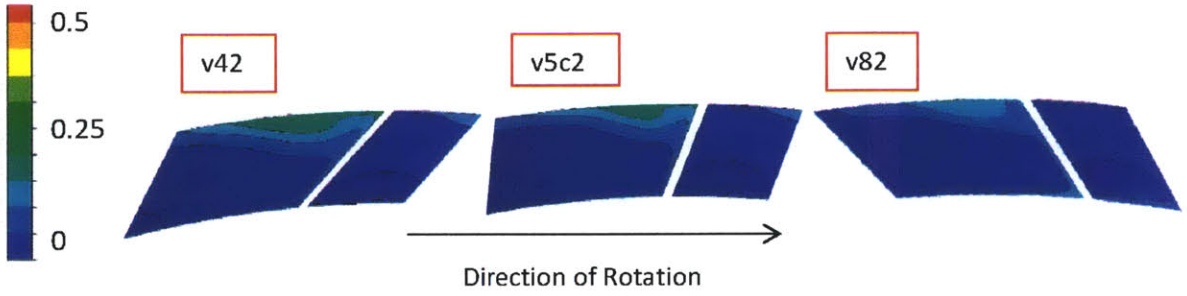

Figure 7-6: Spanwise Distribution of Normalized Entropy showing Wake Region at Trailing Edge

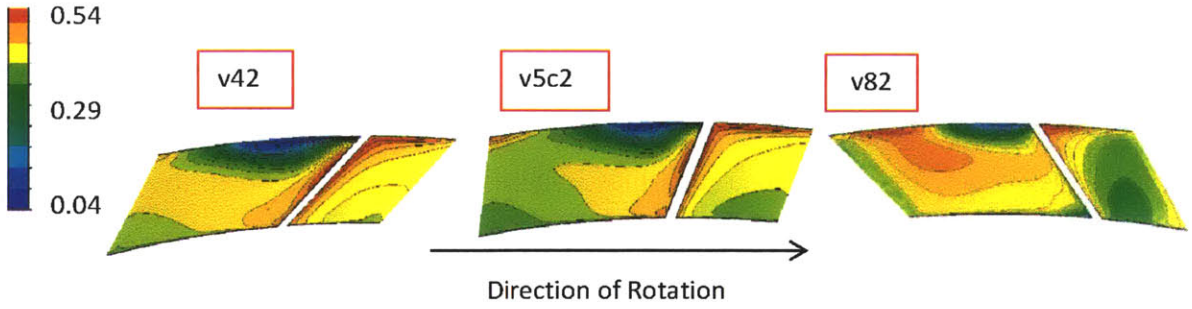

Figure 7-7: Normalized Meridional Velocity $\frac{V_m}{U_2}$ in Wake Region at Trailing Edge

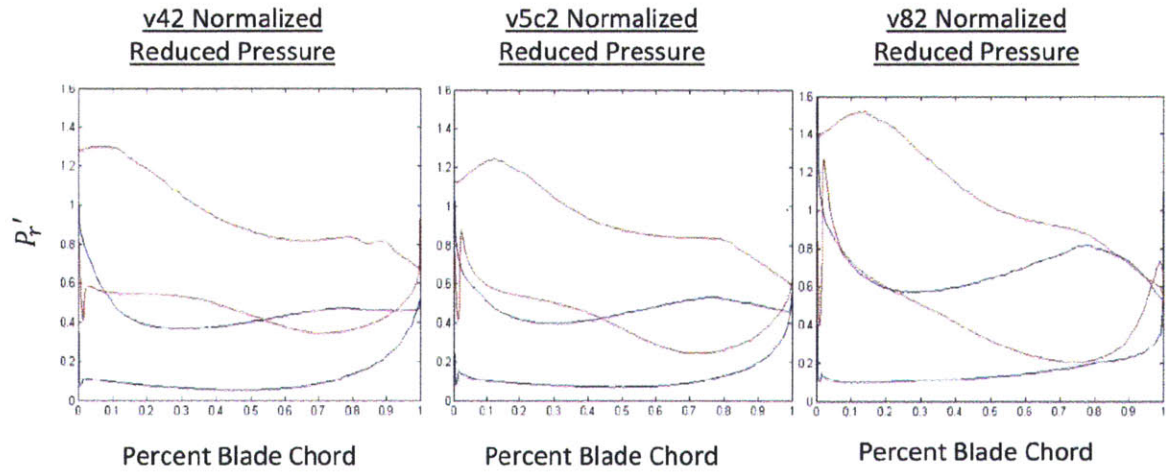

Figure 7-8: Normalized Reduced Pressure on Shroud(Red) and Hub(Blue) for Inlet 2

Figure 7-8 shows the reduced static pressure on the shroud for the inlet 2 cases. Comparing Figure 7-3 to Figure 7-8 shows that the differences in reduced pressure are relatively unaffected (changes of <5%) by the change in inlet curvature. Differences of 10% are seen near 10% blade chord for v8, but the impact is negligible due to negligible secondary flow in this region, as seen in Chapter 6. This is expected as the blade shape is unchanged. The losses for v82 near the trailing edge are reduced by 12%. If the differences in reduced pressure are unchanged, this suggests that the reduction in entropy upstream of the blade leading edge reduces the secondary flow loss along the blade.

7.3 Chapter Summary

In this chapter, it was shown that negative lean for v8 reduces the high entropy region at the trailing edge due to the reduction in hub to shroud secondary flow along the suction surface. The losses on the shroud are thus reduced. The negative lean, however, also increases the pressure to suction side secondary flows, as shown by the increase in ΔC_p, causing a buildup of low momentum fluid in the suction side hub corner. As a consequence, v8 has 6% higher losses than v5c in the post-20% passage length region. The change in inlet affected the gradients in reduced pressure by less than 5% in the post-20% passage length region. The reduction in v82 post-20% passage length losses can be attributed to the reduced inlet loss and decreased secondary flow through the impeller.

Chapter 8

Summary and Future Work

8.1 Summary

(1) Entropy development through the first stage impeller of a multi-stage centrifugal compressor was examined for seven impellers with different blade loading distributions. The impellers were characterized by the amount of front turning, or the turning within the first 20% blade chord, on the shroud. Cases with 60%-80% turning in this region were examined. Three regions of interest were examined: the inlet, the shrouded impeller up to 20% passage length, and post-20% passage length.

(2) Reducing the front turning on the shroud reduced the computed overall losses. The most efficient design reduced overall losses by 8%, compared to the baseline, and had 60% turning in the front 20% blade chord on the shroud. Reduced deceleration in the first 20% of the passage also correlated with reduced overall losses.

(3) The computed inlet loss was 35%-40% of the overall loss. A cause of the losses is a coarse mesh in the inlet bend. Reducing the inlet width reduced the computed dissipation in the mainstream inlet flow by 50%. Higher shroud front loading distributions led to upstream placement of throat and increased upstream dissipation.

(4) The boundary layer state on the blade was analyzed using quasi-3D calculations at 20%, 55%, and 90% span. The results showed that losses at 90% span, near the shroud, correlated with the overall losses in the 3D CFD, ie. the impeller with lowest turning on the casing in the front 20% blade chord had the least overall loss in MISES. Lower front turning moved the peak relative Mach number downstream and reduced the

increase in momentum thickness in the front 10% blade chord. The lower front turning in the front 10% blade chord at 90% span may have potential for reducing overall losses.

(6) Reducing the front turning on the casing made the blade lean more negative (decreased angle between the pressure side and the shroud). Negative lean reduced secondary flow towards the shroud but increased secondary flow toward the suction side. This increased losses in the suction hub corner. Secondary flow was correlated with differences in reduced pressure post-20% passage length between the blade surfaces and the endwalls, although the accumulation of loss on the suction hub corner can outweigh the benefits of reduced suction shroud corner losses.

8.2 Proposed Future Work

Further 3D calculations should be performed on the improved inlet bend and impeller, v82, with the full stage. It was seen that the impeller exit flow of v82 had an improved meridional velocity uniformity compared to the other cases. This typically improves overall stage loss [7], but we did not make this causal connection. The root cause of possible benefits, and level of opportunity, therefore needs to be determined.

Reducing the front loading on the casing in the impeller shows promise in reducing the losses. Additional cases should be tested to confirm this trend.

Appendix A

Turbulence Modelling

The dissipation terms, as seen in Chapter 5, depend not only velocity gradients but also on the eddy viscosity. The SST turbulence model determines these parameters. In flows with high streamline curvature, e.g. bends, experiments show that Reynolds stresses and turbulent kinetic energy are suppressed on the convex side of the bend and amplified on the concave side [17]. In a 90° bend, the SST model, however, has been known to overestimate shear stress on the convex side [19] due to an overprediction of the eddy viscosity.

SST attempts to mitigate this overproduction using Bradshaw's assumption, which states that the shear stress τ in the boundary layer is proportional to the turbulent kinetic energy k [10]:

$$\tau = \rho a_1 k = \mu_t S \tag{A.1}$$

where S is the shear strain rate and a_1=0.31 is an empirically determined value. The shear strain rate is essentially a modified version of the viscous dissipation and is defined as:

$$S = \sqrt{2\left[\left(\frac{du}{dx}\right)^2 + \left(\frac{dv}{dy}\right)^2 + \left(\frac{dw}{dz}\right)^2\right] + \left(\frac{du}{dz} + \frac{dw}{dx}\right)^2 + \left(\frac{dv}{dz} + \frac{dw}{dy}\right)^2 + \left(\frac{du}{dy} + \frac{dv}{dx}\right)^2} \tag{A.2}$$

The eddy viscosity is estimated as [10]:

$$\mu_t = \rho * \frac{a_1 k}{\max(a_1 \omega, SF_2)} \tag{A.3}$$

$$F_2 = \tanh\left(\left(max\left(2 * \frac{\sqrt{k}}{0.09\omega y}; \frac{500\nu}{y^2 \omega}\right)\right)^2\right) \tag{A.4}$$

where ω is the turbulent eddy frequency, y is the distance to the nearest surface, and the second argument is to prevent infinite production of eddy viscosity in the boundary layer. A blending function F_2, which is 1 at the wall and 0 at the midspan, allows the

solver to limit the eddy viscosity in the boundary layer. The use of a blending function is known to cause unrealistic eddy viscosity values [20] at the interface of the models.

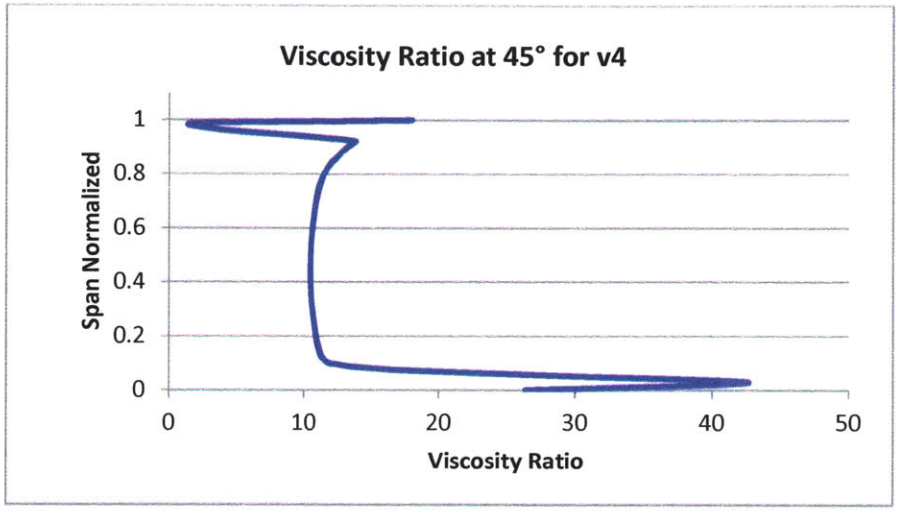

Figure A-1: Viscosity Ratio at 45° for v4

Figure A-1 shows the circumferentially mass-averaged viscosity ratio, μ_t/μ, at the 45° bend location for v4. The viscosity ratio has a value of 10 at the inlet. From 0-10% span, the eddy viscosity increases from the mainstream values approaching a maximum in the boundary layer and decreasing towards the wall. The viscosity ratio is 10-14 in the 10-90% span range. Comparing a streamtube in the boundary layer to a streamtube at the 90% span location containing equal mass, the losses at the 90% span location are 70% less than the losses in the boundary layer at the 45° bend location. Near 90% span, where the mainstream stresses are the highest (as seen in Figure 5-12), the circumferentially mass-averaged normal and shear dissipation terms are 30% of the boundary layer terms, and the eddy viscosity is 30% less than the maximum boundary layer value (See Figure A-1). The flow length for the boundary layer streamtube between the 45° and 90° locations, however, is 50% less than for the 90% span streamtube. The 90% span loss is thus estimated as 65% less than the boundary layer loss.

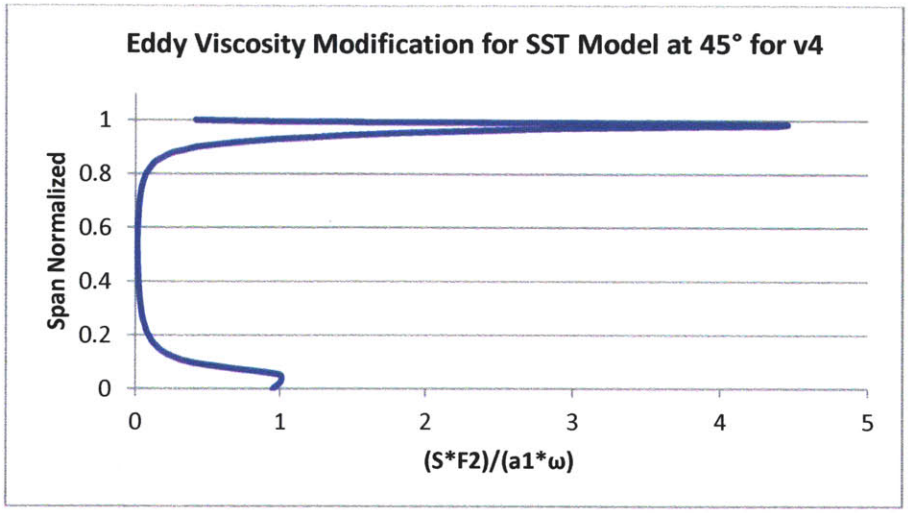

Figure A-2: Eddy Viscosity Modification Factor at 45° for v4

Above 90% span, the eddy viscosity drops from 14 to 2, such that when the eddy viscosity increases in the shroud boundary layer above 98% span, the maximum value is 18, the same order as the mainstream values. The eddy viscosity drop near the shroud can be explained by the solver blending function. Figure A-2 shows the ratio of the denominator terms in the SST eddy viscosity equation. Where, $\frac{SF_2}{a_1\omega} > 1$, in regions of high shear, the eddy viscosity will be limited. This occurs in 90-98% span, outside the boundary layer.

The blending function and the high shear strain rate are responsible for the drop in eddy viscosity and the low eddy viscosity levels in the shroud boundary layer. The meridional and spanwise velocities in Figure A-3 from 45° to 90° show that above roughly 80% span, there is an adverse pressure gradient, whereas the rest of the span sees a favorable pressure gradient. It is known that $k-\epsilon$ overestimates the stress by overestimating the turbulent kinetic energy and underestimating the turbulent dissipation in adverse pressure gradients [19], increasing the length scale in the mainstream and thus leads to higher eddy viscosity levels and mainstream dissipation. Thus it is expected that the mainstream normal and shear stresses undergoing an adverse pressure gradient can allow the solver to overestimate the turbulent length scale near the shroud, generating non-negligible mainstream dissipation.

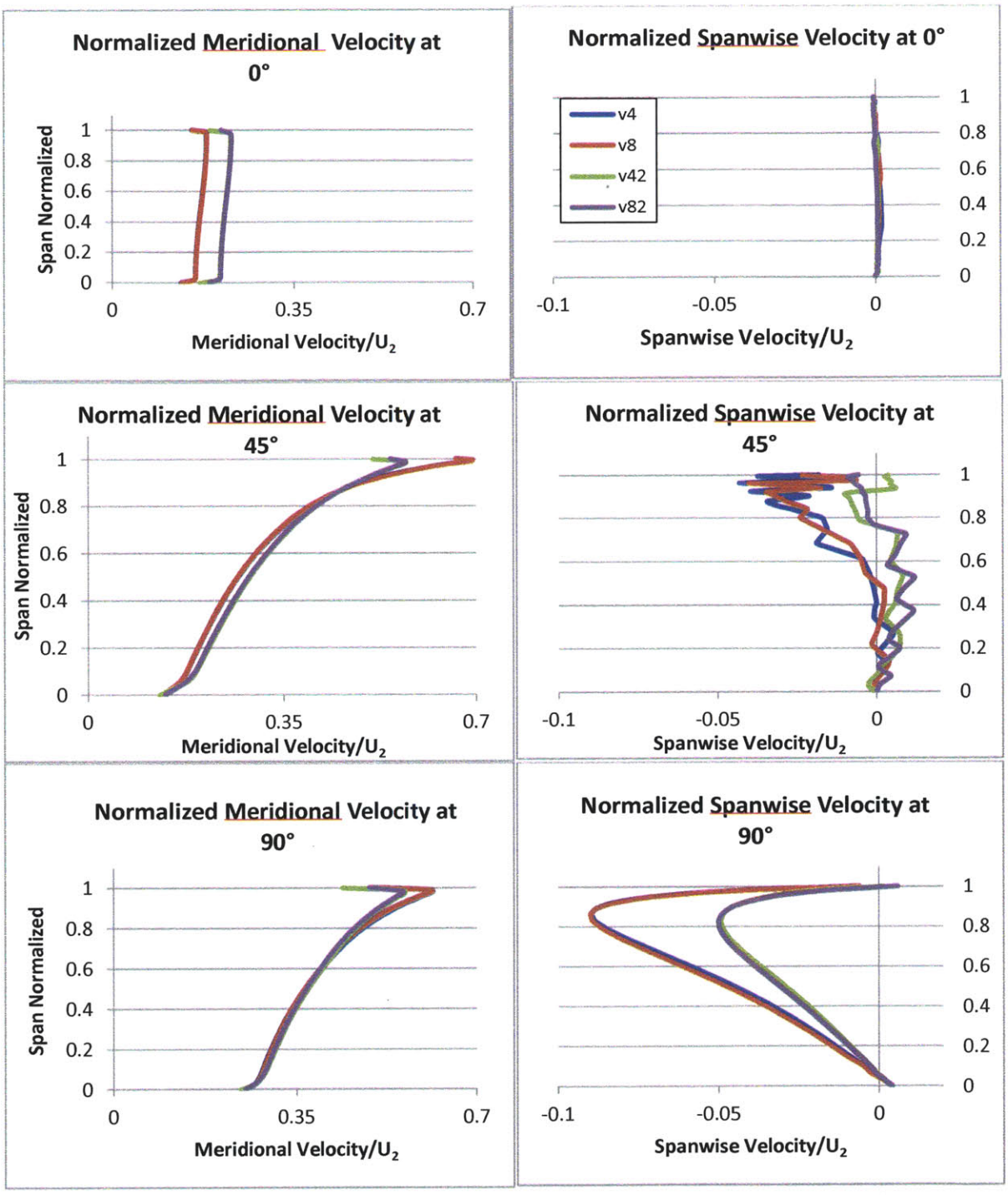

Figure A-3: Normalized Meridional Velocity at (a)0°, (b)45°, and (c)90° and Normalized Spanwise Velocity at (d)0°, (e)45°, and (f)90°.

Figure A-4 shows the viscosity ratio at 45° and 90° for all cases. At 45° and 90°, v82, the case with the least overall entropy rise in the inlet bend, shows twice the eddy

viscosity at the edge of the boundary layer compared to v42, implying that the blade loading distribution affects the eddy viscosity distribution. In the shroud boundary layer above 98% span, v82 shows a viscosity ratio 250% larger than those for the other cases. Increased eddy viscosity in this region allows v82 to have increased resistance to separation.

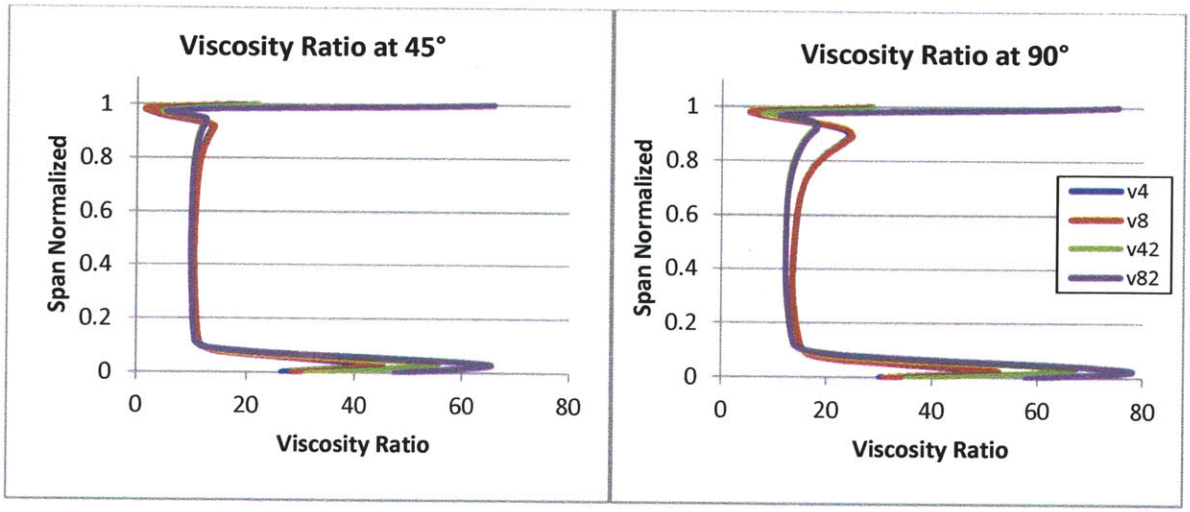

Figure A-4: Viscosity Ratio at (a)45° and (b)90°

Bibliography

[1] Glass B. "Improved Return Passages for Multistage Centrifugal Compressors." Master's Thesis, Massachusetts Institute of Technology, 2010.

[2] Aubry A. "Return Channel Loss Reduction in Multi-Stage Centrifugal Compressors." Master's Thesis, Massachusetts Institute of Technology, 2012.

[3] Sieverding F., Ribi B., Casey M., Meyer M. "Design of Industrial Axial Compressor Blade Sections for Optimal Range and Performance." ASME Journal of Turbomachinery, 2003-GT-38036, 2004.

[4] Walraevens R.E., Cumpsty N.A. "Leading Edge Separation Bubbles on Turbomachine Blades." *ASME Journal of Turbomachinery*, 93-GT-91, 1995.

[5] Calvert W.J., Ginder R.B. "Transonic Fan and Compressor Design." *Proceedings of the Institution of Mechanical Engineers, Part C: Journal of Mechanical Engineering Science*, 213:419, 1999.

[6] Zangeneh M., Goto A., Harada H. "On the Design Criteria for Suppression of Secondary Flows in Centrifugal and Mixed Flow Impellers." *ASME Journal of Turbomachinery,* 97-GT-393, 1998.

[7] Hiradate K., Sugimura K. "Proposal and Experimental Verification of Design Guidelines for Centrifugal Compressor Impellers with Curvilinear Element Blades to Improve Compressor Performance." *Proceedings of ASME Turbo Expo 2014*, GT2014-26642, 2014.

[8] Elliott K.J. "Numerical Investigation of Highly Curved Turbulent Flows in Centrifugal Compressors and in a Simplified Geometry." Master's Thesis, The University of Western Ontario, 2012.

[9] "Innovative Turbulence Modeling: SST Model in ANSYS CFX." Technical Brief, Web. 24 Sept. 2014, <http://www.ansys.com/staticassets/ANSYS/staticassets/resourcelibrary/techbrief/cfx-sst.pdf>.

[10] Menter F. R. "Zonal Two Equation k-omega Turbulence Models for Aerodynamic Flows." *AIAA 24th Fluid Dynamics Conference*, AIAA 93-2906, 1993.

[11] Shibata T., Yagi M. "Effect of Impeller Blade Loading on Compressor Stage Performance in a High Specific Speed Range." *Proceedings of ASME Turbo Expo 2010: Power for Land, Sea, and Air*, GT2010-22281, 2010.

[12] Oh H.W., Yoon E.S., Chung M.K. "An Optimum Set of Loss Models for Performance Prediction of Centrifugal Compressors." *Proceedings of the Institution of Mechanical Engineers,* 211:331, 1997.

[13] McEligot D. M., Walsh E.J., Laurien E. "Entropy Generation in the Viscous Layer of a Turbulent Channel Flow." *5th International Symposium on Turbulence, Heat and Mass Transfer*, INL/CON-06-01272, 2006.

[14] Winter H.H., "Viscous Dissipation Term in Energy Equations." *American Institute of Chemical Engineers Modular Intruction*, Series C, 7:27, 1987.

[15] Holloway A.G.L, Roach D.C., Akbary H. "Combined Effects of Favourable Pressure Gradient and Streamline Curvature on Uniformly Sheared Turbulence." *Journal of Fluid Mechanics*, 526:303, 2005.

[16] Anwer M., So R.M.C., Lai Y.G. "Perturbation by and Recovery from Bend Curvature of a Fully Developed Turbulent Pipe Flow." *Phys. Fluids A 1*, 8:1387, 1989.

[17] Yin J.L., Wang D.Z., Cheng H., Gu W.G. "Assessment of RANS to predict flows with large streamline curvature." *IOP Conference Series: Materials and Engineering 52,* 022002, 2013.

[18] Greitzer, E. M., Tan C.S., Graf M.B. "Internal Flow: Concepts and Applications." New York: Cambridge University Press, 2004.

[19] Rodi W., Scheuerer G. "Scrutinizing the k-epsilon Turbulence Model Under Adverse Pressure Gradient Conditions." *ASME Journal of Fluids Engineering*, 108:174, 1986.

[20] "Use of k-epsilon and k-omega models." Online Posting. Feb 2010. CFD Online. 25 Sept. 2014. <http://www.cfd-online.com/Forums/main/75554-use-k-epsilon-k-omega-models.html>.

[21] Shahinfar S., Fransson J.H.M. "Effect of Free-Stream Turbulence Characteristics on Boundary Layer Transition." *Journal of Physics: Conference Series 318*, 032019, 2011.

[22] Brandt L., Schlatter P., Henningson D.S. "Transition in boundary layers subject to free-stream turbulence." *Journal of Fluid Mechanics*, 517:167, 2004.

[23] Drela M., Youngren H. "A User's Guide to MISES 2.67." As of Sept. 2008.

[24] Menter F., Carregal Ferreira J., Esch T., Konno B., "The SST Turbulence Model with Improved Wall Treatment for Heat Transfer Predictions in Gas Turbines." *Proceedings of the International Gas Turbine Congress 2003 Tokyo*, IGTC2003-TS-059, 2003.

[25] Kang S, Hirsch C. "Numerical Simulation and Theoretical Analysis of the 3D Viscous Flow in Centrifugal Impellers." *Task Quarterly 5*, 4:433, 2002.

[26] Denton J.D. "Loss Mechanisms in Turbomachines." *Journal of Turbomachinery*, 115:4, 1993.

[27] Farge T. Z., Johnson M.W. "Effect of flow rate on loss mechanisms in a backswept centrifugal impeller." *International Journal on Heat and Fluid Flow*, 13:189, 1992.